2023

QUANTIFYING THE EVOLUTION OF STRENGTHENING MECHANISMS FOR COMMERCIALLY PRODUCED NIOBIUM AND TITANIUM HSLA STEEL SHEET

Isabella M.W. Jaszczak
Michigan Technological University, imwakeha@mtu.edu

QUANTIFYING THE EVOLUTION OF STRENGTHENING MECHANISMS FOR COMMERCIALLY PRODUCED NIOBIUM AND TITANIUM HSLA STEEL SHEET

By

Isabella M.W. Jaszczak

A THESIS

Submitted in partial fulfillment of the requirements for the degree of

MASTER OF SCIENCE

In Materials Science and Engineering

MICHIGAN TECHNOLOGICAL UNIVERSITY

2023

This thesis has been approved in partial fulfillment of the requirements for the Degree of MASTER OF SCIENCE in Materials Science and Engineering.

Department of Material Science and Engineering

Thesis Advisor:	*Dr. Paul G. Sanders*
Committee Member:	*Dr. Erico T. F. Freitas*
Committee Member:	*Dr. Matthew Enloe*
Department Chair:	*Dr. Walter Milligan*

Table of Contents

Table of Contents iii
Acknowledgements v
Abstract vi
1 Introduction & Background 1
1.1 High-Strength, Low-Alloy Steels 1
1.1.1 Bulk Production of HSLA Hot-Rolled Sheet 2
1.1.2 Mechanical Property Stability in Commercial HSLA steels 4
1.2 Strengthening Mechanisms of Steels 6
1.2.1 Solid Solution Strengthening 7
1.2.2 Hall-Petch Strengthening 8
1.2.3 Geometrically Necessary Dislocation Strength 9
1.2.4 Precipitation Strengthening 12
1.3 Titanium & Niobium in HSLA Steels 15
1.3.1 Titanium & Niobium Precipitation Behavior 15
1.3.2 Niobiums Role in the Deceleration of Austenite Softening 16
1.3.3 Austenite to Ferrite Transformation 19
1.3.4 Thesis Hypothesis 20
2 Experimental Methods 21
2.1 Sample Composition & Information 21
2.2 EBSD Sample Preparation 23
2.3 EBSD Mapping 23
2.4 Metallography 24
2.5 Carbon Extraction Replica 25
2.6 STEM Imaging & Analysis 26
2.7 Thermo-Calc Modelling 27
2.8 Volume Fraction Calculation 27
3 Results 28
3.1 Solid Solution Strength 28
3.2 Hall-Petch Strength 28
3.3 Dislocation Strength 30
3.4 Precipitation Strengthening 31
3.5 Total Predicted Strength 34
4 Discussion 36
4.1 Coil Temperature & Location Effect on Strength 36

4.1.1 Hall-Petch Strength..... 36
4.1.2 Dislocation Strength..... 37
4.1.3 Shear & Orowan Precipitate Strength..... 38
4.1.4 Summed Precipitate Strength..... 43
4.2 Hypothesis Analysis..... 44
5 Conclusions..... 46
6 Reference List..... 47

Acknowledgements

There have been many people who have blessed me with knowledge, advice, patience, and motivation throughout this project; I am incredibly thankful for their guiding hands I felt continuously over the past year.

"There is only one way to eat an elephant: a bite at a time."

- ***Desmond Tutu; Regularly quoted by my late swim coach JL.***

Thank you to Dr. Paul Sanders for his advisorship and support. His dedication to all students is admirable and always finds a way to motivate people to achieve their full potential.

Thank you to CBMM for their financial support of this project and guidance from Dr. Ana Araujo.

Thank you to Dr. Matthew Enloe and Kyle Vanover from Steel Dynamics Inc for reviewing project progress, sharing steel minimill wisdom, and providing samples.

Thank you to Dr. Erico Freitas and Elizabeth Miller for patiently teaching me crucial sample preparation and imaging techniques I needed for this project.

Thank you to Dr. Stephen Kampe, Dr. Douglas Swenson, Dr. Dale Dewald, and Tom Wood for their advising in material science theory.

Thank you to Eli Harma for being a superb office-mate and a great listener. He helped brainstorm the way through project hiccups regularly.

Thank you to the Wakehams, Jaszczaks, McKilligans, Strayers, and Neelys; I am so lucky for their kinship and friendship that is a foundation in my life.

Abstract

Strength uniformity along the coil length of commercially produced high-strength, low-alloy (HSLA) steel hot-rolled sheet is crucial to avoid the downgrading of product that does not meet strength specifications. In addition to contributing to precipitation strengthening through the growth of niobium-titanium carbides ((Nb,Ti)-C), niobium hinders austenite recrystallization and refines ferrite grain size. The potency of these strengthening mechanisms relies heavily on the austenite to ferrite transformation kinetics of the hot-rolling process. While niobium's effect on precipitation strengthening, Hall-Petch strengthening, dislocation strengthening, and solute strengthening have all been studied in literature independently, the interactions of these mechanisms with each other and coiling temperature in a commercial production setting is not completely understood. The strengthening behavior of niobium microalloyed HSLA steels compared to a non-niobium HSLA steel is quantified and correlated using commercially produced samples and a design of experiments with factors coil temperature and location on coil length. Hall-Petch grain size strengthening and geometrically necessary dislocation strengthening are determined from electron backscatter diffraction mapping. Orowan precipitation strength is quantified from image analysis of (Nb,Ti)-C precipitates captured on carbon extraction replica films using a scanning transmission electron microscope. Solubility of alloying elements in the ferrite matrix, and therefore solute strengthening, is calculated with Thermo-Calc. This study observed that niobium supported a trend of increased Orowan strength to balance the decrease in Hall-Petch strength that occurred as coiling temperature increased.

1 Introduction & Background

1.1 High-Strength, Low-Alloy Steels

High-strength, low-alloy (HSLA) steels are low-carbon, micro-alloyed steels that act as the transition material between high ductility, low-strength and low ductility, ultra-high strength steels (Figure 1.1.1) [1]. A HSLA steel's formability, weldability, and strength are greatly dependent on the material's microalloying elements such as niobium (Nb), titanium (Ti), molybdenum (Mo), and vanadium (V) in weight quantities of ~0.01 wt% to 0.1 wt% [2].

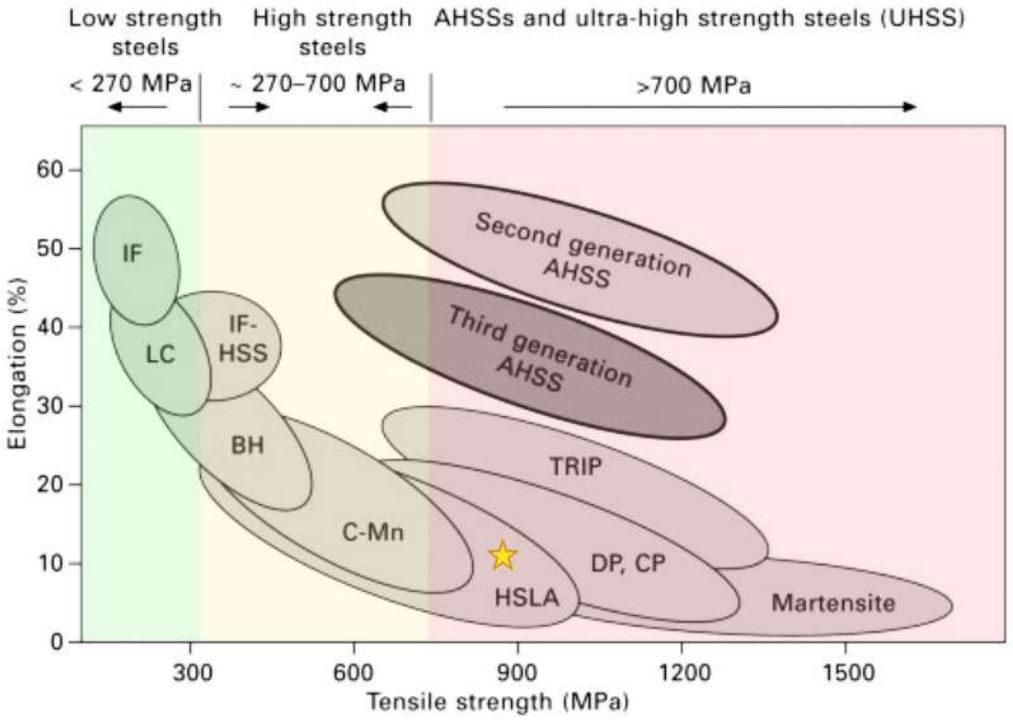

Figure 1.1.1 Strength vs ductility Ashby plot showing the progression of steels that have high ductility and low-strength to low ductility and ultra-high strength. HSLA steels reside in the middle of these extremes [1].

1.1.1 Bulk Production of HSLA Hot-Rolled Sheet

HSLA steel is an essential component of U.S. manufacturing including the automotive, structural, energy, and transportation industries [2]. A majority of U.S. commercial vehicles' have HSLA steel body components as of 2019 [3]. HSLA steel used in manufacturing or construction are typically formed from a bulk geometry such as sheet or slab.

Compact strip production (CSP) in steel minimills manufacture these products in a four-step process: melt, cast, roll, and coil (Figure 1.1.2). While the melt step is where the heat's chemistry is adjusted, the casting, rolling, and coiling steps have the greatest effect on the steel's microstructure [2]. After melting in an electric arc furnace, the molten steel is cast into a slab form through continuous casting. During continuous casting, the molten steel is gravity-fed into a water-cooled mold which solidifies an outer shell of the steel, while the inner core continues to solidify farther down the casting segments. Once the slab is at the target initial rolling temperature, the slab undergoes a multipass hot rolling process to reduce its thickness. With each rolling step, the steel is gradually cooled to its finishing temperature, or the temperature the steel is during its final rolling pass. This point is also around the temperature that yields the austenite to ferrite phase transformation [4]. The sheet is then quickly cooled to a coiling temperature that initiates the austenite to ferrite transformation and is coiled on a mandrel (Figure 1.1.3).

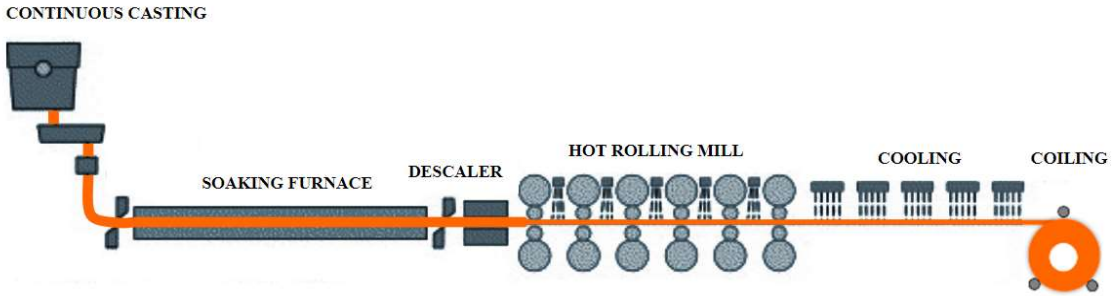

Figure 1.1.2 Bulk produced steel products produced in a minimill follow a process similar to the one depicted in the diagram. Following melt processes, the steel is cast, rolled and coiled to its final form in one continuous process [5].

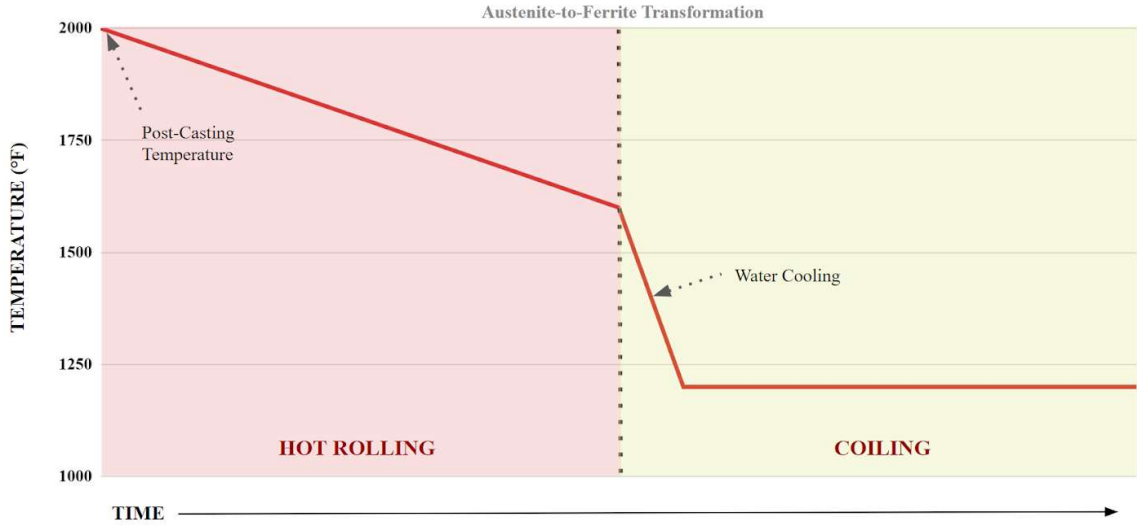

Figure 1.1.3 Example thermal profile for hot-rolled HSLA steels; rolling passes during hot rolling decrease temperature of steel to its finishing temperature just above the austenitization temperature. Water cools the sheet to its final coiling temperature.

The ~20-50 ton coils are then left to air cool for multiple days prior to quality checks of the mechanical properties. Typically, 30 ft. “head” and “tail” portions of the coil are removed prior to mechanical testing due to differences in microstructure (Figure 1.1.4).

Despite this, it is not uncommon that the split section of the coils show strength variation stemming from the cooling profile of the coils [6].

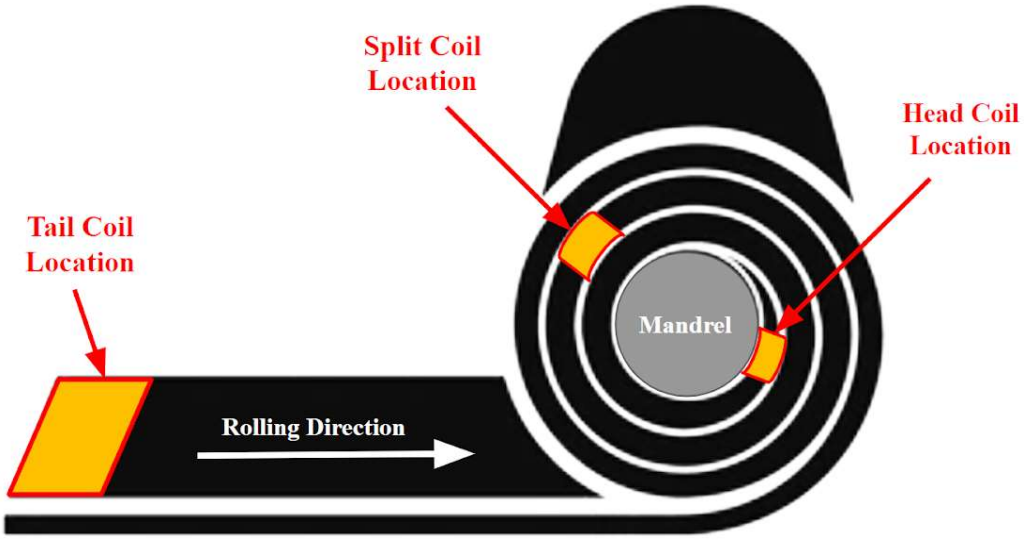

Figure 1.1.4 Diagram showing the coil locations of head, split, and tail in reference to the rolling direction of the sheet and mandrel.

1.1.2 Mechanical Property Stability in Commercial HSLA steels

The common micro-alloying additions of Nb, Ti, V, and Mo all contribute to improved strength through the formation of carbide precipitates, grain refinement, dislocation strengthening, and solute strengthening. The retention of these additions' potential strengthening can change with varying thermal processing conditions. Temperatures at the casting, rolling, and coiling may vary by ~200°F, leading to slightly different microstructures.

If the resulting HSLA steel microstructure does not have uniform mechanical properties that meet strength grade standards, the product will not meet customer specifications and is unfit for intended use [6]. As a result, it must be downgraded or recycled. This is neither economical nor efficient for steel mills and their customers.

Steel mills have observed a clear improvement in mechanical property uniformity in 100 ksi grade HSLA steels that contain niobium and titanium in juxtaposition to HSLA steels with only titanium as the key strengthening element (Figure 1.1.5). Nb-Ti HSLA steels exhibited an average strength variation of ~4 ksi while Ti HSLA steel samples had ~10 ksi of variation [6]. The goal of this research is to quantify changes in strengthening mechanisms for Nb-Ti HSLA steel sheet samples coiled at different temperatures to better explain this phenomena. The specific mechanisms included in this thesis are solid solution strengthening, Hall-Petch strengthening, dislocation strengthening, and precipitation strengthening. Quantifying niobium's improvements to HSLA steel strength uniformity will justify the use of niobium in commercial production of HSLA steel.

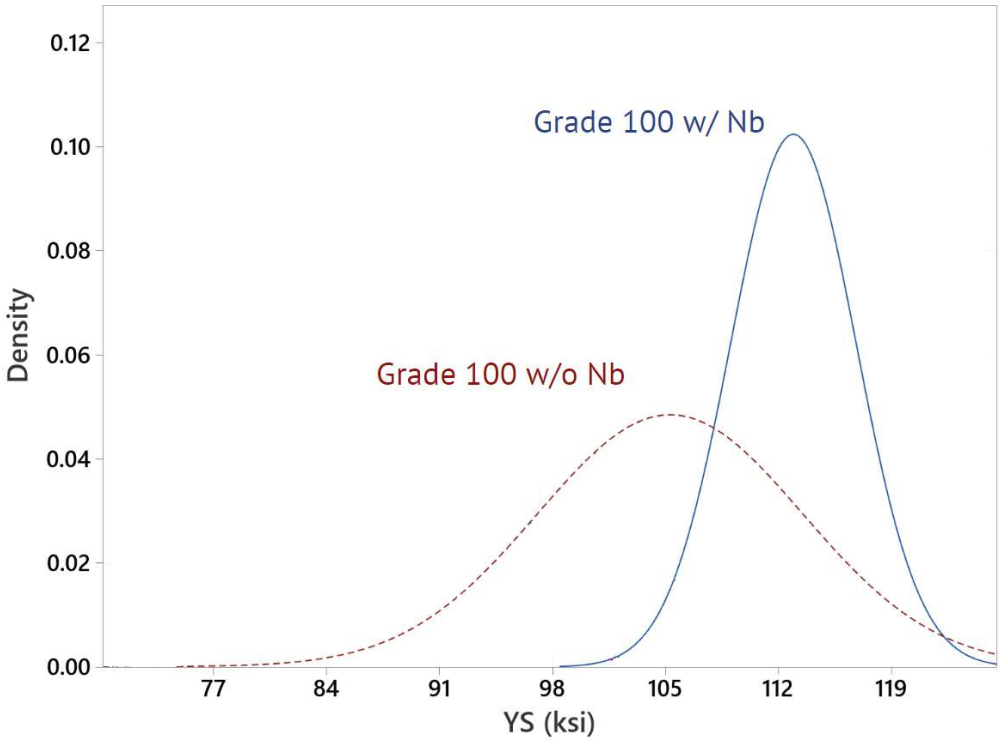

Figure 1.1.5 Comparison of yield strength distributions for grade 100 ksi HSLA with and without niobium shows that Nb-Ti HSLA steels have significantly less variation than Ti HSLA steels [6].

1.2 Strengthening Mechanisms of Steels

Impeding dislocation motion and the mechanisms in which dislocations overcome obstacles are the fundamental mechanisms for strengthening of metals. Dislocations are line defects in a crystal lattice that disrupt the long-range order of atoms in a material. Two canonical types of dislocations exist: edge and screw dislocations. Edge dislocations occur when an extra half-plane of atoms is inserted into the crystal lattice, while screw dislocations result from a shear distortion where the lattice is displaced along a line. Most materials contain a mix of these dislocation types [7].

Under the application of stress, dislocations can move and therefore enable the plastic deformation of the material at lower strengths than the theoretical bond strength. The strength of a metal directly correlates to how easily dislocations can move; when the motion of dislocations is hindered, the metal becomes stronger [7]. Several microstructure features act as obstacles for dislocation motion including solute atoms, grain boundaries, other dislocations, and precipitates. Alloy chemistry, heat treatments and deformation processes are designed to maximize these obstacles in HSLA steels. The more obstacles that are present, the more difficult it is for dislocations to travel, therefore increasing the yield strength of the material.

This concept of hindering dislocation motion is the basis of the four key strengthening mechanisms of metals: solution strengthening (σ_{SSS}), Hall-Petch grain size strengthening (σ_{HP}), work hardening (σ_{GND}), and precipitation strengthening (σ_{PPT}). Through modeling, EBSD, and image analysis, these mechanisms can be quantified and summed to estimate the total strength of the material when added to the base frictional lattice strength (σ_o) value for HSLA steel of 54 MPa (Equation 1.2.1) [8]. Foreman and Makin found that the most accurate way to sum strength contributed by dislocations and precipitates is to average via the pythagorean theorem to avoid overestimation of strength [9]. This is to best account for the observed mix of obstacle strengths and densities that affect the calculated strength contribution from dislocation and precipitate obstacles. Base

frictional lattice stress, solid solution particles and grain boundaries are intrinsic traits of the overall polycrystalline matrix of a material and therefore are summed normally..

$$\sigma_{TOTAL} = \sigma_o + \sigma_{SSS} + \sigma_{HP} + \sqrt{\sigma_{GND}^2 + \sigma_{PPT}^2} \qquad 1.2.1$$

1.2.1 Solid Solution Strengthening

Alloying elements in steel that do not explicitly participate in the formation of ferrite or carbides will occupy interstitial or substitutional positions in the crystal lattice. This will cause lattice distortion and create strain fields that impede the motion of dislocations, thereby increasing the yield strength of the material. The amount of strengthening depends on factors such as concentration of solute atoms and their atomic size difference relative to the matrix atoms (Figure 1.2.1) [7].

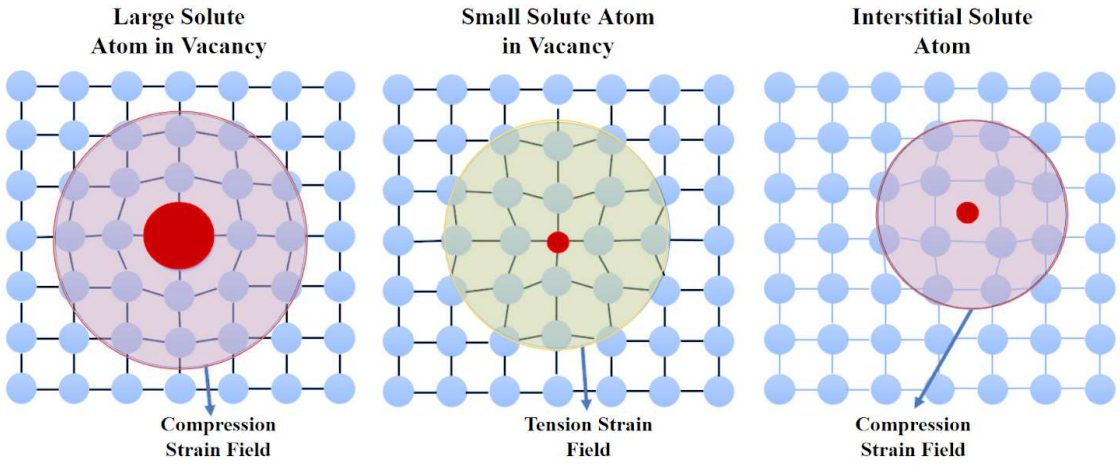

Figure 1.2.1 Diagram showing how different solute atom sizes and sites may affect the surrounding crystal lattice to create a strain field [10].

For HSLA steels, micro-alloying elements such as manganese (Mn), silicon (Si), and molybdenum (Mo) are most potent in contributing solid solution strength [11]. The lighter elements carbon and nitrogen are consumed by the formation of precipitates and therefore contribute limited solid solution strength; strength that is provided by these elements is represented in the base frictional lattice strength.

Table 1.2.1 Strength increase for common HSLA steel solid solution strengthening elements by weight [11].

Element	Increase in σ_{YS} per 1 wt. % (MPa)	Increase in σ_{UTS} per 1 wt. % (MPa)
Mo	+11	+45
Si	+85	+85
Mn	+32	+28

1.2.2 Hall-Petch Strengthening

The Hall-Petch equation describes the inverse relationship between grain size and strength in polycrystalline materials:

$$\sigma_{HP} = \frac{K}{\sqrt{d}} \qquad 1.2.2$$

The parameter σ_{HP} is the estimated strength contribution, K is the Hall-Petch constant, and d is the average grain diameter. Average grain diameter can be assessed through electron backscatter diffraction (EBSD) mapping. The Hall-Petch constant for HSLA steels is 600 MPa for high-angle grain boundaries [12].

Grain boundaries act as barriers to dislocation movement due to differences in neighboring grains' misorientation which increases the energy needed to facilitate motion across grain boundaries. Dislocation pile-up at boundary sites leads to high stress fields that can eventually activate dislocations from grain-to-grain [7]. As grain size decreases

in a material, the number of these obstacles increases (Figure 1.2.2). The increase in the yield stress stems from this increased energy requirement for dislocation motion across the entire microstructure. By controlling the grain size through thermal and deformation processing techniques, the mechanical properties of steel can be tailored to achieve desired strength and ductility requirements.

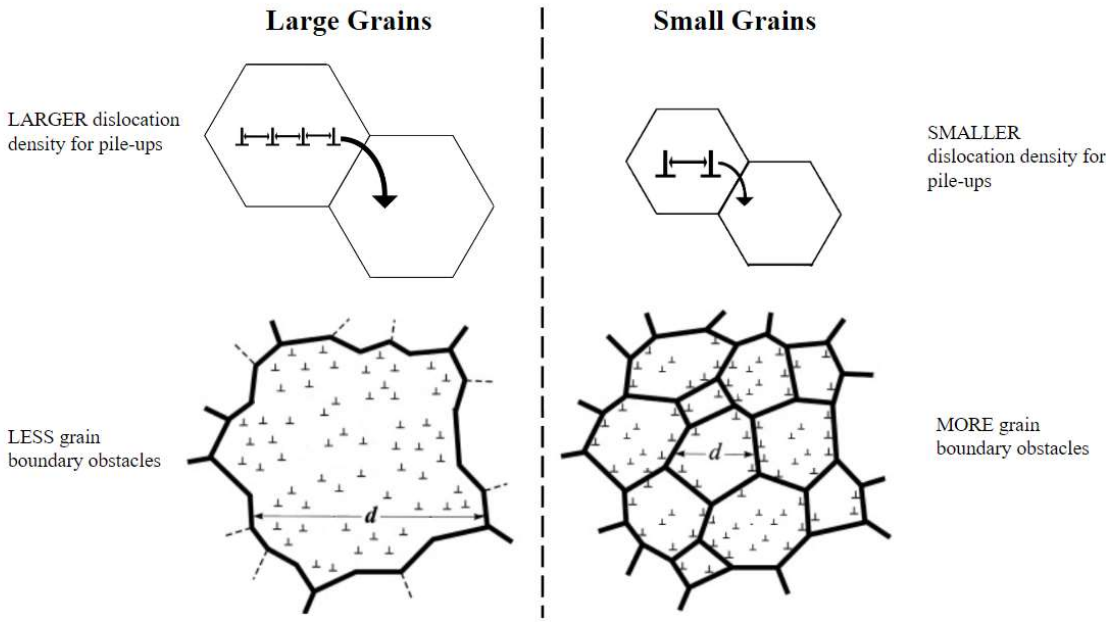

Figure 1.2.2 Finer grains benefit material strength by possessing more dislocation obstacles as well as having a reduced dislocation number density to facilitate dislocation pile-up [13].

1.2.3 Geometrically Necessary Dislocation Strength

Polycrystalline materials have two key types of dislocations that form with deformation. Statistically stored dislocations (SSDs) describe the random accumulation of dislocations within a grain during deformation. Geometrically necessary dislocations GNDs are dislocations specifically induced to accommodate changes in the grain's geometry from deformation and occur near grain boundaries or other heterogeneous microstructure

features [14]. GNDs are significantly more potent than SSDs in strengthening a material through dislocation tangling and pile-up due to their greater strain in the grain's lattice [15].

The theory behind GND strengthening is linked to the concept of dislocation entanglement and the Taylor hardening law. When a material undergoes deformation, dislocations move and interact, leading to the formation of dislocation structures such as tangles. The presence of a high density of GNDs creates a complex dislocation network that impedes dislocation motion, thereby increasing the strength of the material [16].

The density of GNDs can be quantified using kernel average misorientation (KAM) data, which is typically obtained through EBSD. A KAM data point is a measure of the average misorientation of the measured area defined by the EBSD scan step size relative to its neighbors areas that do not lay on a grain boundary. EBSD procedures studied by Calcagnotto et al. revealed that using second neighbor misorientation measurements instead of first neighbor KAM measurements yields higher contrast in KAM measurements (Figure 1.2.3) [16]. This is due to more neighbors being included in KAM calculations done by EBSD software.

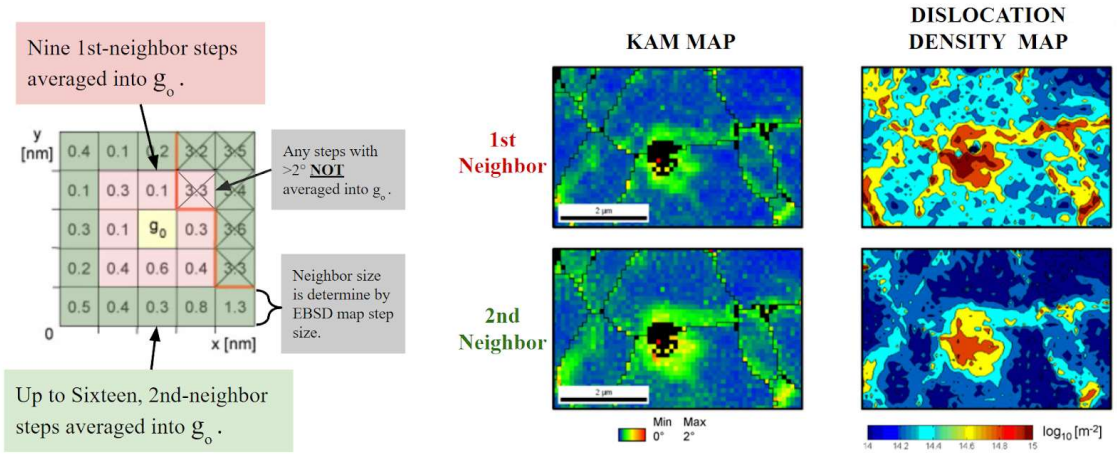

Figure 1.2.3 EBSD KAM measurements are calculated by averaging the misorientation of neighboring scanned areas. By using second neighbor measurements, more data points are used to calculate the KAM data and contrast is increased for KAM maps and dislocation density maps [16].

This provides a more accurate KAM values to be used to calculate dislocation density. The relationship between KAM and GND density is given by the equation below where ρ_{GND} is the GND density, β is a constant related to the presence of tilt or twist boundaries, θ is the kernel average misorientation, b is the Burgers vector magnitude, and μ is the scanning step size used for EBSD (Equation 1.2.3).This calculated density is then used in the Taylor hardening equation to estimate the strength contribution from GNDs (σ_{GND}) where α is a constant, M is the Taylor Factor, G is the shear modulus of the material, and b is the Burgers vector (Equation 1.2.4) .

$$\rho_{GND} = \frac{\beta * \theta}{b * \mu} \qquad 1.2.3$$

$$\sigma_{GND} = \alpha M G b \sqrt{\rho_{GND}} \qquad 1.2.4$$

Values for the parameters for these equations can be found in literature (Table 1.2.2). In HSLA steels, a value of 3 should be used for β to represent the mix of tilt (β=2) and twist (β=4) boundaries observed for the material.

Table 1.2.2 Literature values for ρ_{GND} and σ_{GND} equation parameters.[17]

Parameter	Value for 100 Grade HSLA Steel
β	3
b	0.250 nm
α	0.3
M	3
G	64 GPa

1.2.4 Precipitation Strengthening

Precipitation strengthening occurs with the formation of small, finely distributed particles, or precipitates, within the matrix during thermal processing. Precipitates are obstacles that dislocation must consume energy to overcome via mechanisms like Orowan looping and shearing, therefore increasing the strength of the material (Figure 1.2.4). The effectiveness of precipitation strengthening relies on the size, distribution, and volume fraction of these precipitates[18]. In a ferrite matrix, (Nb,Ti)C must nucleate in a coherent, low interfacial energy orientation. These nuclei will subsequently grow larger than their critical nucleus size at a given temperature and become incoherent with the matrix [17], [19]. This transition between coherency/incoherency also dictates the shearable/non-shearable precipitate size for NbC carbides in HSLA steels.

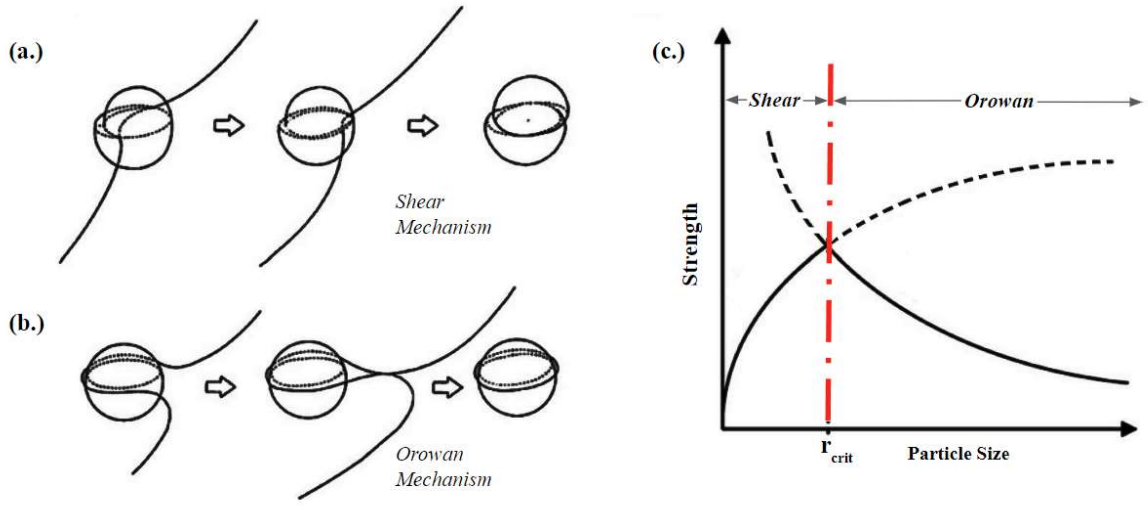

Figure 1.2.4 For precipitates smaller than r_{crit} (c), dislocation bypass the obstacle via shearing (a). When the precipitate is larger than r_{crit} (c), the dislocation forms and pinches off an Orowan loop as it travels around the precipitate (b) [20].

The Orowan strengthening mechanism generally applies to precipitates that are incoherent with the matrix; these precipitates can be distinguished by having a radius $>r_{crit}$ [19]. Dislocations are unable to shear through the precipitates due to the incoherent interface and size. Instead they create a loop around each precipitate in order to continue its trajectory [18]. A high volume fraction of small, evenly-dispersed precipitates will strengthen a material significantly while coarse, localized precipitates provide much less strengthening. The yield strength increase due to the Orowan mechanism can be calculated using Equation 1.2.5, where $\lambda_{e\text{-}e}$ is the mean spacing between the precipitates (Equation 1.2.6), R is the mean radius, ƒ is the volume fraction of precipitates, M is the Taylor factor, G is the shear modulus, b is the magnitude of the Burgers vector, and ν is Poisson's ratio (Table 1.2.3).

$$\sigma_{oro} = \frac{0.4MGb\ ln(\frac{2R}{b})}{\pi\ \lambda e{-}e\ \sqrt{1-\nu}} \qquad 1.2.5$$

$$\lambda_{e\text{-}e} = R\left(\sqrt{\frac{2\pi}{3f}} - \frac{\pi}{2}\right) \qquad 1.2.6$$

Table 1.2.3 Literature values for σ_{oro} equation parameters.

Parameter	Value for 100 Grade HSLA Steel
b	0.250 nm
υ	0.28
M	3
G	64 GPa

The shearing mechanism for overcoming coherent precipitates ($r<r_{crit}$) consists of dislocations shearing through the obstacle. Quantifying the energy needed to facilitate this mechanism is not as clear as calculating Orowan strength. Charleux et. al. outlines a method for estimating precipitate shearing strength for NbTi HSLA steels and determined a value for relative obstacle strength [17], in which *D* is the is the mean coherent precipitate diameter, f is the volume fraction of precipitates, *M* is the Taylor factor, *G* is the shear modulus, *b* is the magnitude of the Burgers vector, and *Γ* is obstacles relative strength constant (Equation 1.2.5/Table 1.2.4).

$$\sigma_{shear} = \frac{2MGb\sqrt{f}}{\sqrt{\pi}D}\ \Gamma^{\ 2/3} \qquad 1.2.5$$

Table 1.2.4 Literature values for σ_{shear} equation parameters[17].

Parameter	Value for 100 Grade HSLA Steel
b	0.250 nm
M	3
G	64 GPa
Γ	0.18

1.3 Titanium & Niobium in HSLA Steels

1.3.1 Titanium & Niobium Precipitation Behavior

For the HSLA steel samples in this study, two types will be discussed: titanium nitrides (TiN) and niobium-titanium carbides ((Nb,Ti)C)[17]. Of these two precipitates, TiN precipitates first as available titanium is used to draw nitrogen out of solid solution. These cubic precipitates are coarse and are ~1 μm in size; due to their large size, they do not typically strengthen the material. Remaining titanium and niobium will form fine (Nb,Ti)C precipitates that nucleate at grain boundaries or along dislocation dense regions with average diameters of ~10-50 nm and ~4 nm respectively. Their size and distribution make them Orowan or shear strengthening particles and improve the alloy's ductility by consuming carbon from solid solution [17].

Titanium will have the tendency to form nitrides, sulfides, and oxides before forming carbides; for the alloys in this study, niobium does not share this behavior and nearly all available niobium will form carbides (Figure 1.3.1) [21]. This difference in compound formation likely contributes to niobium-containing HSLA steels having improved strength as niobium will not interact in-solution nonmetal elements except to form favorable carbides. For titanium, there must be the appropriate excess atoms available beyond the N+O+S composition to form carbides.

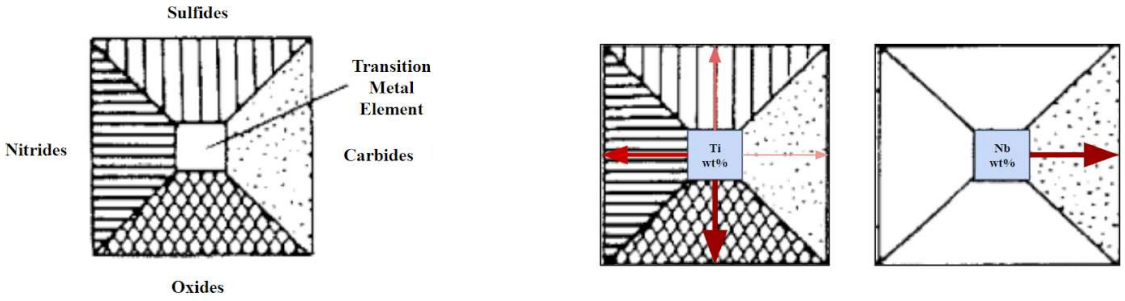

Figure 1.3.1 During nucleation and growth of precipitates in steels, titanium has the tendency to form oxides, nitrides, and sulfides prior to forming carbides. Niobium tends to form carbides or carbonitrides immediately. Width and hue of arrows is proportional to formation tendency of each nonmetal compound [21].

1.3.2 Niobiums Role in the Deceleration of Austenite Softening

Niobium slows austenite recrystallization during hot deformation via two mechanisms: initially with solid drag followed by precipitation of niobium carbides along dislocation fronts. Literature has shown that while other alloying elements such as vanadium and titanium follow a similar strengthening route, niobium hinders softening more dramatically. In the early stages of hot deformation, when the steel is at high temperatures ~2000°F, niobium exists in solid solution in the austenite phase. It contributes to slowing the softening mechanisms of recovery and recrystallization more potently than other common micro-alloying elements (Figure 1.3.2) [21]. When carbon is present to form NbC precipitates, recovery and recrystallization is suppressed more potently than in-solution niobium (Figure 1.3.3). While the reasoning for this phenomenon is still being understood, initial studies suggest that early supersaturation of NbC precipitates in austenite during hot deformation pins grain boundaries (Figure 1.3.4) [21].

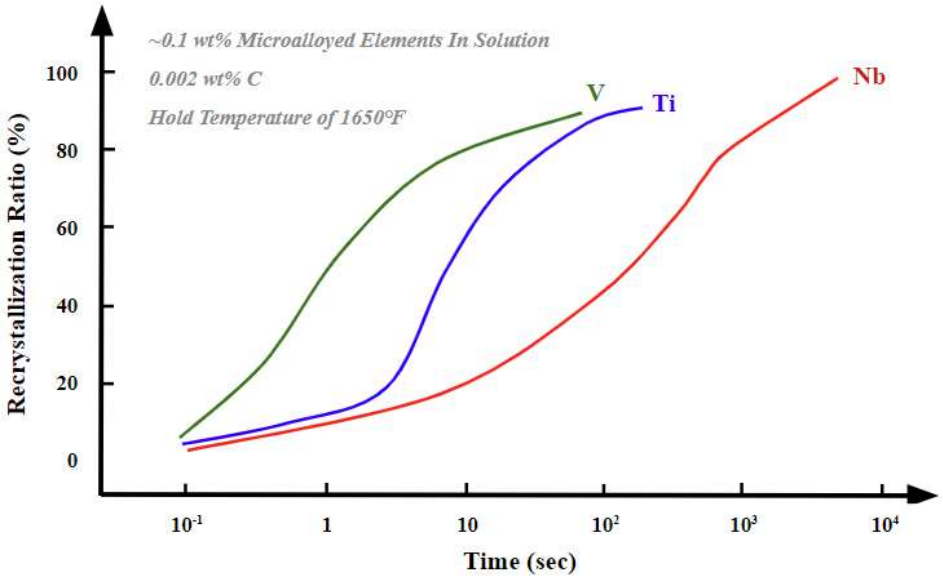

Figure 1.3.2 For a steel alloy held at 1650°F and a carbon wt% of 0.002, niobium delayed austenite softening via recrystallization a full order of magnitude longer than Ti, the next best performing alloying element [21].

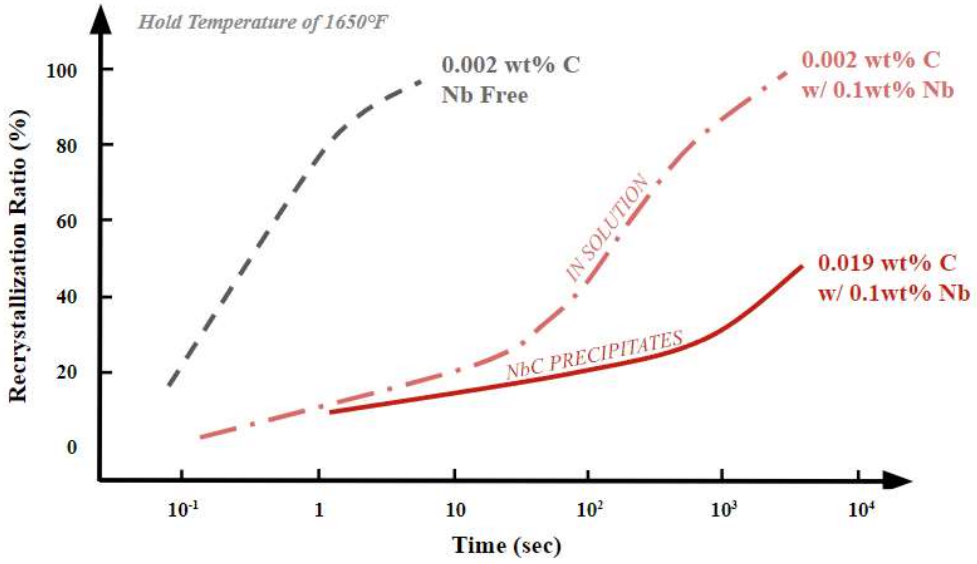

Figure 1.3.3 For a steel alloy held at 1650°F with varying carbon compositions showed the precipitation of NbC precipitates delayed recrystallization and reduced the recrystallized ratio more potently that in-solution niobium [21].

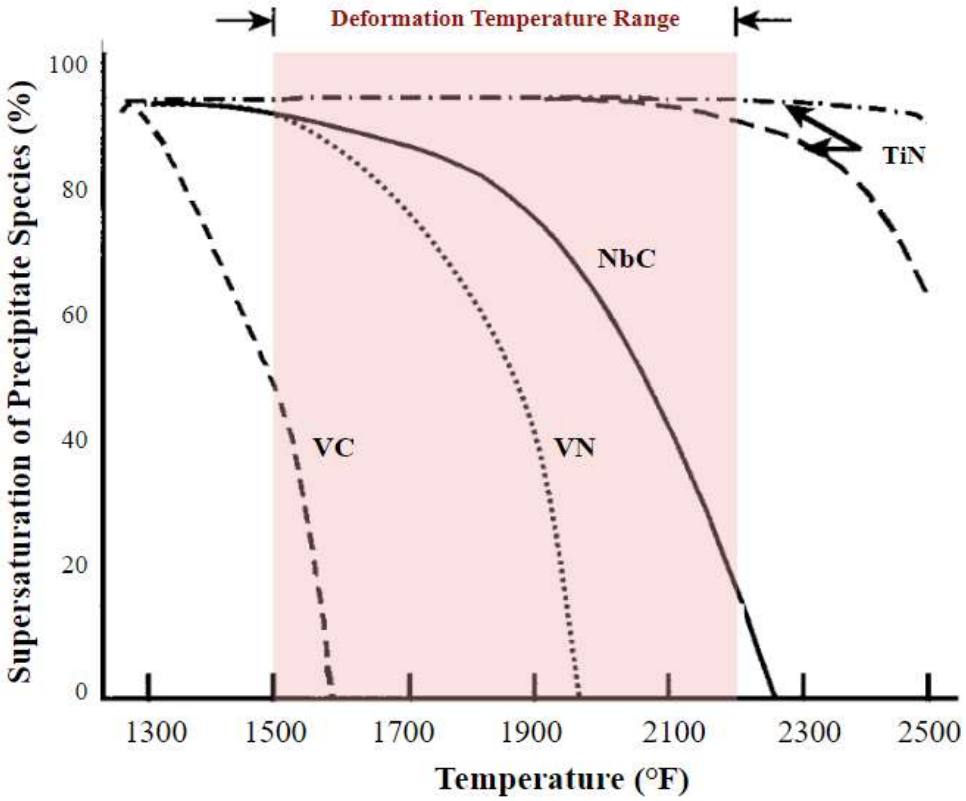

Figure 1.3.4 As a steel alloy is cooled from casting temperatures through hot deformation temperatures, TiN precipitates out the fastest of the studied precipitates. NbC is the next quickest to precipitate out leading to a high saturation of strengthening particles during deformation [21].

As the steel sheet cools to the austenite-to-ferrite transformation temperature with each reduction pass, more niobium precipitates out of solution to form fine NbC precipitates as both solubility decreases and nucleation sites at high dislocation density areas increase. These nucleation sites tend to be at or near the grain boundary due to dislocation pile-ups. Titanium would have to form other compounds first such as TiN that will only slow softening if precipitated out at high slab cooling rates.

1.3.3 Austenite to Ferrite Transformation

Upon cooling below the austenite-to-ferrite transformation temperature for coiling, niobium's increased mobility in ferrite leads to the immediate nucleation and growth of any remaining Nb, Ti, and sometimes Mo solute (Figure 1.3.5). This is due to the face-centered cubic to body-centered cubic transformation that occurs at the austenitization temperature that allows for faster substitutional diffusion [21].

As the ferrite structure stabilizes, precipitates that had nucleated prior-to and after the austenite-to-ferrite transformation grow. The temperature the material is held at during coiling controls how much solute niobium, titanium, and carbon can diffuse. The size these precipitates reach determines if they will strengthen the matrix via shearing or Orowan looping. Precipitates smaller than the r_{crit} are coherent and therefore strengthened by shearing; precipitates larger than r_{crit} are incoherent with the matrix and strengthened by looping. For HSLA steels with an austenitizing temperature at 2000°F, Gagliano et. al. determined a r_{crit} value of ~2.5 nm [19].

(Nb,Ti)C precipitates utilize the phase transformation front as a nucleation site within the intra-grain region. These precipitates and the presence of the NbC precipitates formed at hot rolling temperatures impede dislocation movement and lead to a high retained dislocation density. The resulting ferritic grain structure is influenced by this; structures typical of high cooling rate such as acicular ferrite and bainitic ferrite can form at lower cooling rates. Research has even observed high dislocation densities in standard polygonal ferrite in niobium HSLA steels subjected to intermediate to slow cooling rates [21].

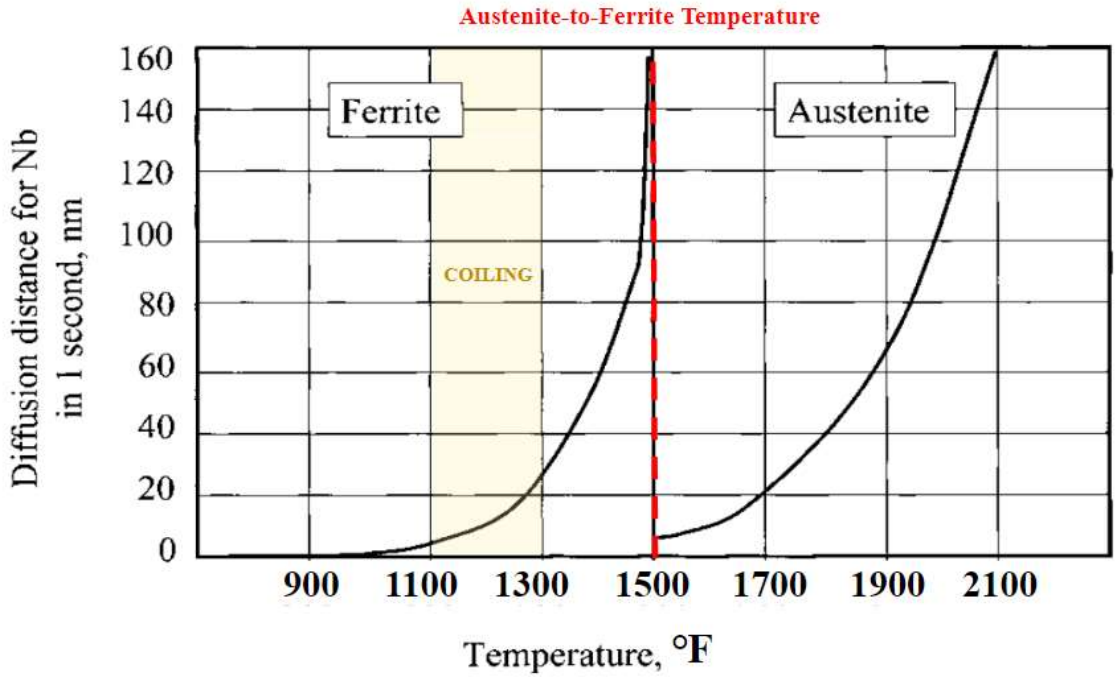

Figure 1.3.5 Modeled max travel of niobium solute in austenite and ferrite for 1 second of travel time [21]. Note that the niobium diffusion distance is the same order of magnitude in ferrite as in pearlite, even though the temperature is significantly lower.

1.3.4 Thesis Hypothesis

Overall, it is well studied that niobium decelerates softening in austenite during rolling processes that leads to an optimal microstructure for the austenite-to-ferrite transformation. This project's goal is to track the changes in strengthening that occur during and after this transformation at coiling temperatures commonly used in minimills. If hot-rolled HSLA steel is micro-alloyed with niobium, then mechanical properties will be more uniform despite variations in coiling temperature because niobium will increase precipitation strengthening at higher temperatures where dislocation strength and grain size strength decrease.

2 Experimental Methods

2.1 Sample Composition & Information

Nine niobium-titanium alloyed 100 grade HSLA steel sheet samples for each 2-factor, 3-level DOE condition were provided by CBMM that were manufactured at Steel Dynamics Inc's Butler, IN mini-mill (Table 2.1.1, 2.1.2). A single 100 grade HSLA steel baseline centerpoint sample was provided with the key strengthening element being titanium; this sample is from the split location of a coil coiled at 1200°F. Samples were labeled according to the following scheme: SampleComposition_CoilTemperature_CoilLocation.

Table 2.1.1 Design of Experiments Factors and Levels

Factor	Level 1	Level 2	Level 3
Coil Temperature	1100°F	1200°F	1300°F
Coil Location	Head	Split	Tail

Table 2.1.2 Composition wt% of HSLA Steel Samples

Sample Composition Label	Nb	Ti	C	Mn	P	S	Si	Al	Cu	Ni	Cr	Mo
NbTi	0.012	0.114	0.045	0.396	0.0108	0.0009	0.303	0.042	0.079	0.029	0.161	0.205
Ti	0.002	0.128	0.049	0.372	0.0091	0.0010	0.187	0.041	0.077	0.032	0.072	0.188

All samples were hot-rolled at a target finishing temperature of 1600°C in a series of seven reduction passes to a final thickness of 0.13''; the material was then water quenched and coiled at the specified temperature. Following coiling, the coils, weighing between 18-24 tons, were air cooled prior to sectioning (Figure 2.1.1). Samples were not sectioned from coils with high precision; therefore coil location has some variation.

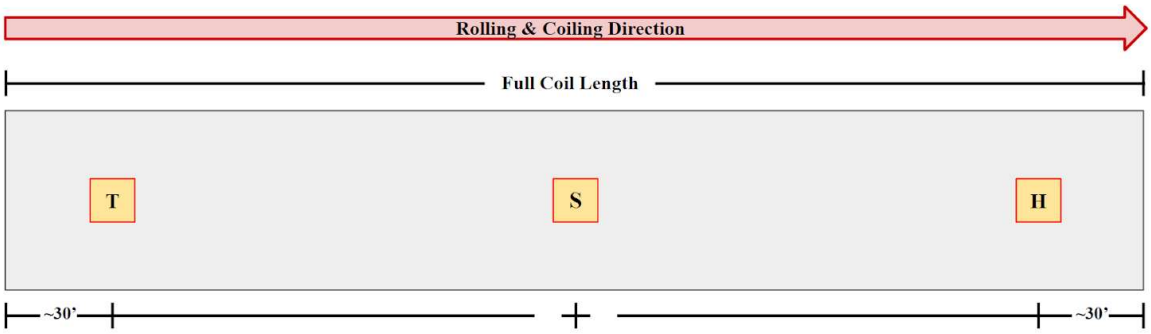

Figure 2.1.1 Head and tail samples were sectioned from the middle of the sheet's width at the approximate location of 30' from respective locations' end; the split samples were taken from the middle of the sheet's width at the center of the coil's length.

All analyses included in this study assessed the microstructure of the HSLA steel perpendicular to the rolling direction (RD) (Figure 2.1.2). This orientation correlates to the samples tensile tested by Steel Dynamics Inc for this study and is the strongest microstructure orientation for wrought materials.

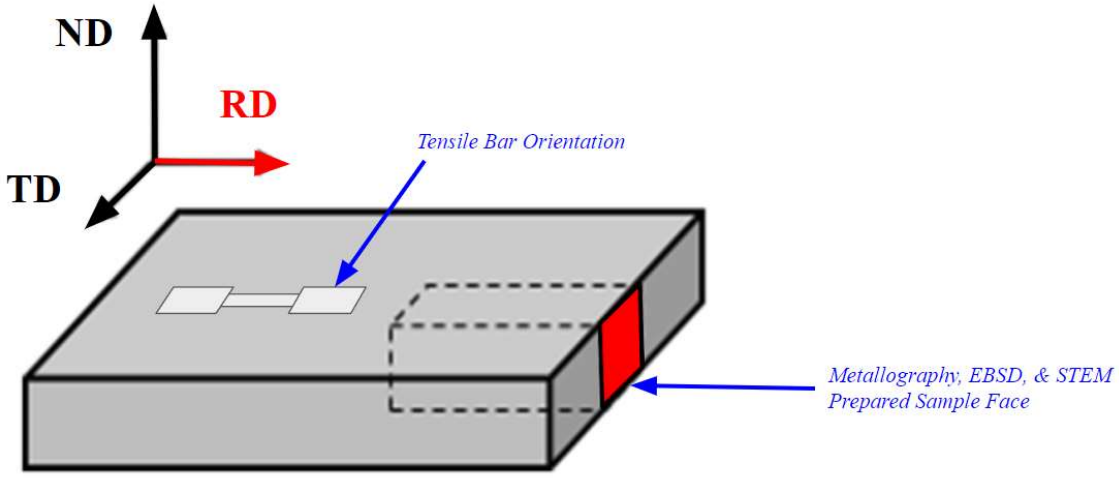

Figure 2.1.2 Orientation diagram for all metallographic and CER samples.

2.2 EBSD Sample Preparation

Three 0.5’’x 0.25’’ rectangles were cut with a hydraulic shear for each DOE condition with the long edge perpendicular to the rolling direction. The RD face of the EBSD samples were ground flat with 600 grit SiC grinding pads on a LECO VP-150 manual polishing station. A JEOl IB-09010CP Cross Section Polisher at Michigan Tech was used to mill the samples’ surface prior to EBSD mapping (Table 2.2.1). Milled samples were then adhered to an aluminum EBSD stub using carbon cement.

Table 2.2.1 Jeol IB-09010CP Cross Section Polisher settings for HSLA steel EBSD samples.

Polisher Model	Mode	Voltage	Ar Gas	Time
Jeol IB-09010CP	Rotating Mill	6.0 kV	3.9	6 hrs

2.3 EBSD Mapping

EBSD samples were assessed using a FEI Philips XL 40 environmental scanning electron microscope with both Oxford Instruments AZtec acquisition software and HKL Channel 5 EBSD analysis software (Table 2.3.1). Per DOE condition, enough EBSD maps were collected to meet the grain analysis guidelines of ASTM E2627 standard; mapping concluded once data for >2000 grains was collected per DOE condition (Table 2.3.2). The only phase included in indexing was BCC iron.

Table 2.3.1 ESEM and AZtec software settings used for EBSD mapping.

SEM Model	Accelerating Voltage (keV)	Spot Size	Magnification	EBSD Step Size
FEI Philips XL 40	20 keV	6.5	2500x	0.2 μm

Table 2.3.2 ASTM E2627 EBSD guidelines compared to metrics used.

	Minimum Average Pixel Resolution per Grain	Maximum Zero Solution w/o Cleaning	Minimum Grains Analyzed
ASTM E2627	100	10%	500
Project Method	100	10%	2000

Maps were collected from the circular milled region of the EBSD samples at the 1/3rd and 2/3rd thickness locations along the HSLA sheet's thickness to map areas of average grain size for the sample type (Figure 2.3.1).

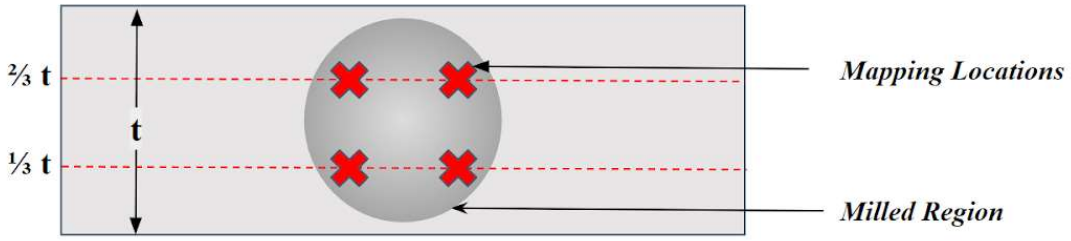

Figure 2.3.1 EBSD mapping regions for grain and misorientation data collection on the rolling direction (RD) surface of sample shown in Figure 2.1.2.

2.4 Metallography

Two mounts were created for each sample type for optical microscopy and carbon extraction replica (CER) sample preparation. A hydraulic shear was used to cut six 1''x 0.5'' rectangles per DOE condition; the 1'' length was cut perpendicular to the rolling direction. Three rectangles were mounted in cross-section in a single 1.25'' diameter bakelite mount. Samples were ground and polished using a ten-mount Buehler Ecomet 4 Autoplosher (Table 2.4.1). A 2% Nital etch was used to reveal grain structure for optical metallography using the FEI Philips XL 40 environmental scanning electron microscope.

Table 2.4.1 Manual Metallography Steps for HSLA Steel Samples

Abrasive	Speed (rpm)	Pressure (lbs)	Time (s)	Pad Type
120 grit	200	35	Until planar	SiC
320 grit	200	35	60	SiC
600 grit	200	35	60	SiC
800 grit	180	35	60	SiC
1200 grit	180	25	90	SiC
1 μm diamond paste	150	20	240	Allied Kempad
0.05 colloidal silica	150	20	120	Allied Final P

2.5 Carbon Extraction Replica

The CER process was used to make carbon films for STEM imaging (Figure 2.5.1). For STEM imaging, tweezers and 300 mesh copper TEM grids were used to remove films from the distilled water wash beaker.

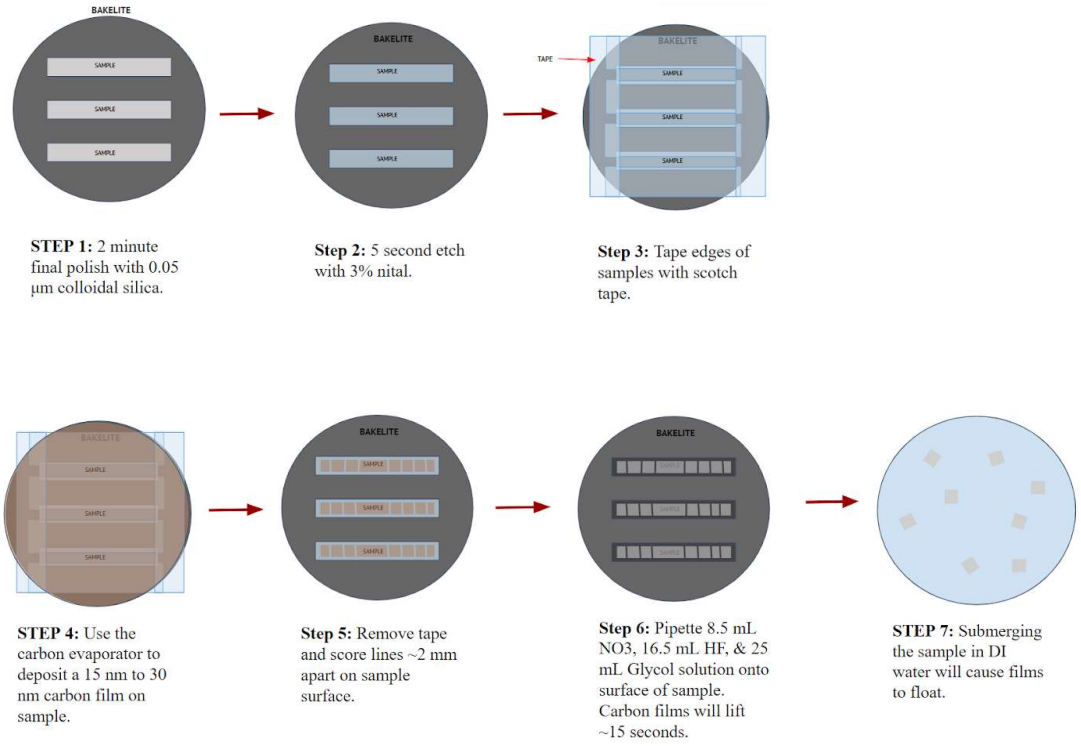

Figure 2.5.1 Process flow chart for CER process used for STEM sample preparation.

2.6 STEM Imaging & Analysis

CER films were imaged using a FEI 200kV Titan Themis scanning transmission electron microscope (STEM) at Michigan Technological University in conjunction with the Velox acquisition software; an operating voltage of 200 kV using a double tilt specimen holder was used. Samples were secured with copper washers and clips.

Table 2.6.1 STEM settings used for STEM imaging.

STEM Model	Accelerating Voltage (kV)	Spot Size	Magnification
FEI 200kV Titan Themis	200 kV	6.0	400kx

The Count-and-Measure feature of the Olympus Stream Essentials software was used to measure carbide diameter and area from collected STEM images. Images were analyzed until >1000 precipitates were characterized.

2.7 Thermo-Calc Modelling

The single point equilibrium function from the ThermoCalc 2022b software was used to calculate the composition of the ferrite matrix (BCC_A2#1) and (Nb,Ti)(C,N) precipitates (FCC_A1#2, FCC_A1#4, FCC_A1#5). Ferrite composition output was used for solid solution strength calculations. (Nb,Ti)(C,N) precipitate volume fractions were used for precipitate strength calculations.

Table 2.7.1 Thermo-Calc Single Point Equilibrium Conditions

Run	Composition	Equilibrium Temperature
1	NbTi	1100°F
2	NbTi	1200°F
3	NbTi	1300°F
4	Ti	1200°F

2.8 Volume Fraction Calculation

Of the volume fraction of (Nb,Ti)(C,N) precipitates calculated in Thermo-Calc, only the fraction of precipitates with a carbon atom occupying the nonmetal sites were used in volume fraction estimates for precipitate strength calculations.

To separate the coherent and incoherent precipitates fractions from the total modeled volume fraction of (Nb,Ti)C, data from the STEM image analysis was also factored in. A fraction of coherent and incoherent particles was determined from the distribution of precipitate areas. The critical radius value of 2.5 nm from literature was used to distinguish the two precipitate types.

(Nb,Ti)(C,N) Fraction * (Nb,Ti)(C) Fraction * Coherent/Incoherent Fraction = Vf,(Nb,Ti)C 2.8.1

3 Results

3.1 Solid Solution Strength

Thermo-Calc single point equilibrium calculations yielded estimates of alloying elements in solution for the NbTi and Ti sample types (Table 3.1.1). These compositions in conjunction with Equation 3.1.1 were used to calculate solid solution strength contributions.

Table 3.1.1 Modeled wt.% Composition of Ferrite Matrix for HSLA Steel Samples

Sample Composition Label	Mn	Si	Mo	Solid Solution Strength
NbTi_1100	1.362	0.304	0.128	45
NbTi_1200	1.372	0.304	0.168	46
NbTi_1300	1.302	0.304	0.207	47
Ti_1200	1.337	0.188	0.166	36

$$\sigma_{SSS} = 11\ \text{MPa} * \text{wt\% Mo} + 85\ \text{MPa} * \text{wt\% Si} + 32\ \text{MPa} * \text{wt\% Mn} \quad 3.1.1$$

3.2 Hall-Petch Strength

Hall-Petch strength was characterized for all samples using Equation 1.2.2 and collected EBSD data (Table 3.2.1, Figure 3.2.1). The only NbTi sample with a weaker Hall-Petch strength than the Ti-only sample was NbTi_1300_Head.

Table 3.2.1 Average Grain Size & Hall-Petch Strength with 95% Propagated Error

Sample Label	Coil Temp. (°F)	Coil Location	Average Grain Size [ECD] (um)	Hall-Petch Strength (MPa)
NbTi_1100_Head	1100	Head	2.17 ± 0.06	408 ± 8
NbTi_1100_Split	1100	Split	2.16 ± 0.05	408 ± 5
NbTi_1100_Tail	1100	Tail	2.07 ± 0.06	417 ± 6
NbTi_1200_Head	1200	Head	2.29 ± 0.06	396 ± 3
NbTi_1200_Split	1200	Split	2.31 ± 0.06	395 ± 5
NbTi_1200_Tail	1200	Tail	2.41 ± 0.05	387 ± 4
NbTi_1300_Head	1300	Head	2.25 ± 0.05	400 ± 4
NbTi_1300_Split	1300	Split	2.58 ± 0.07	374 ± 5
NbTi_1300_Tail	1300	Tail	2.72 ± 0.07	364 ± 5
Ti_1200_Split	1200	Split	2.60 ± 0.07	372 ± 5

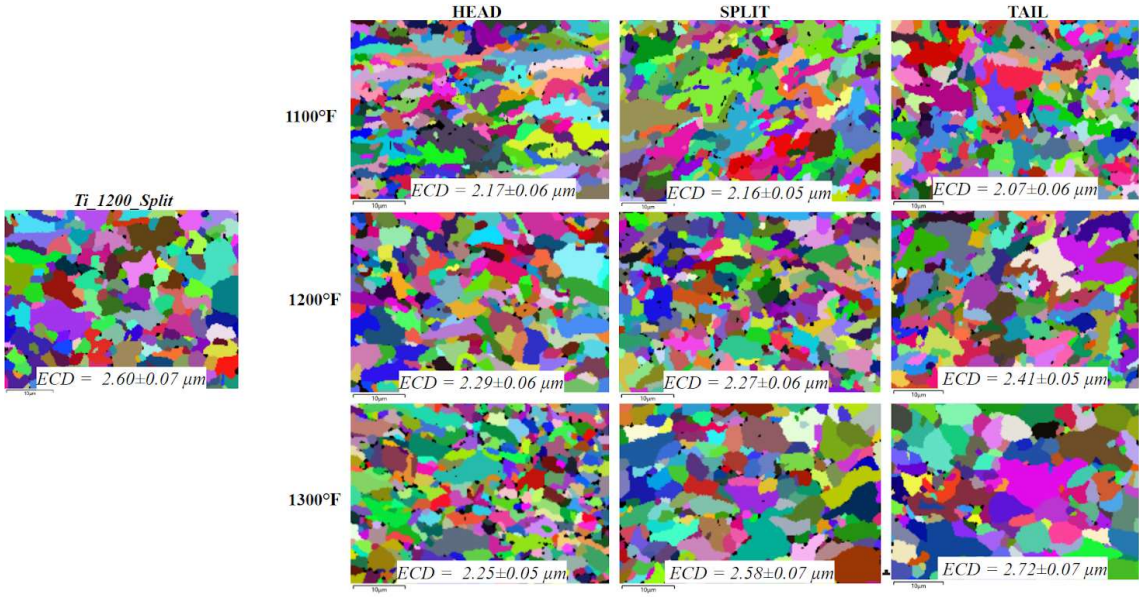

Figure 3.2.1 Grain maps from EBSD for Ti control sample and DOE samples.

3.3 Dislocation Strength

KAM data <2° collected during EBSD was used to calculate dislocation strength using equation 1.2.3 and 1.2.4. The Ti_1200_Split control sample had the lowest dislocation strength out of all samples.

Table 3.3.1 Dislocation Strength with 95% Propagated Error

Sample Label	Coil Temp. (°F)	Coil Location	Average Misorientation (°)	GND Dislocation Density (dislocation per m^2)	Dislocation Strength (MPa)
NbTi_1100_Head	1100	Head	0.543±0.001	1.508E+14	129.7 ± 0.3
NbTi_1100_Split	1100	Split	0.545±0.001	1.522E+14	130.3 ± 0.3
NbTi_1100_Tail	1100	Tail	0.518±0.001	1.447E+14	127.0 ± 0.3
NbTi_1200_Head	1200	Head	0.398±0.001	1.112E+14	111.3 ± 0.3
NbTi_1200_Split	1200	Split	0.514±0.001	1.435E+14	126.5 ± 0.3
NbTi_1200_Tail	1200	Tail	0.392±0.001	1.094E+14	110.4 ± 0.3
NbTi_1300_Head	1300	Head	0.668±0.002	1.870E+14	144.4 ± 0.3
NbTi_1300_Split	1300	Split	0.498±0.001	1.391E+14	124.6 ± 0.3
NbTi_1300_Tail	1300	Tail	0.492±0.001	1.351E+14	122.7 ± 0.2
Ti_1200_Split	1200	Split	0.314±0.001	8.756E+13	98.8 ± 0.2

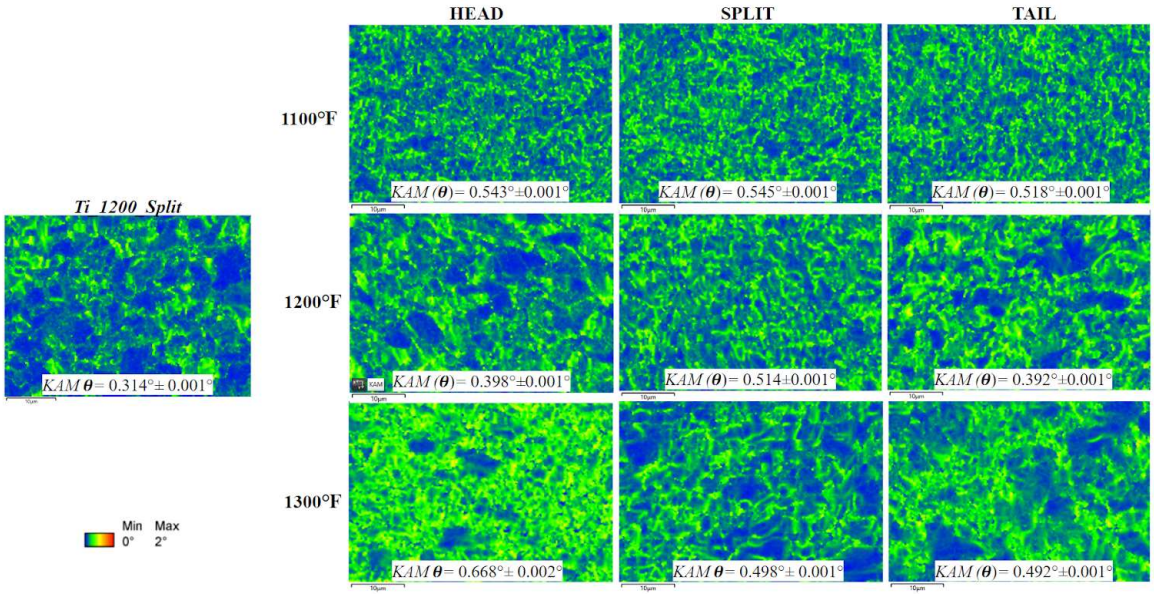

Figure 3.3.1 Kernel average misorientation maps from EBSD for Ti control sample and DOE samples.

3.4 Precipitation Strengthening

All CER films assessed contained (Nb,Ti)C precipitates (Figure 3.4.1, Table 3.4.1). Total precipitate strength was calculated via a pythagorean sum to adhere to Equation 1.2.1 (Table 3.4.2).

Table 3.4.1 Precipitate Summary with 95% Propagated Error

Sample Label	Coil Temp. (°F)	Coil Location	Coherent Precipitate Radius (nm)	Coherent Precipitate Volume Fraction	Incoherent Precipitate Radius (nm)	Incoherent Precipitate Volume Fraction
NbTi_1100_Head	1100	Head	0.77±0.16	0.00098	3.99±0.86	0.00079
NbTi_1100_Split	1100	Split	1.27±0.14	0.00104	3.33±0.13	0.00079
NbTi_1100_Tail	1100	Tail	1.43±0.30	0.00115	3.13±0.52	0.00062
NbTi_1200_Head	1200	Head	0.82±0.03	0.00076	3.55±0.13	0.00091
NbTi_1200_Split	1200	Split	0.76±0.03	0.00089	3.31±0.17	0.00077
NbTi_1200_Tail	1200	Tail	0.76±0.03	0.00105	3.01±0.09	0.00062
NbTi_1300_Head	1300	Head	1.24±0.11	0.00090	3.75±0.23	0.00106
NbTi_1300_Split	1300	Split	1.13±0.08	0.00044	3.66±0.11	0.00152
NbTi_1300_Tail	1300	Tail	0.90±0.08	0.00088	3.35±0.11	0.00108
Ti_1200_Split	1200	Split	0.77±0.06	0.00079	3.36±0.18	0.00112

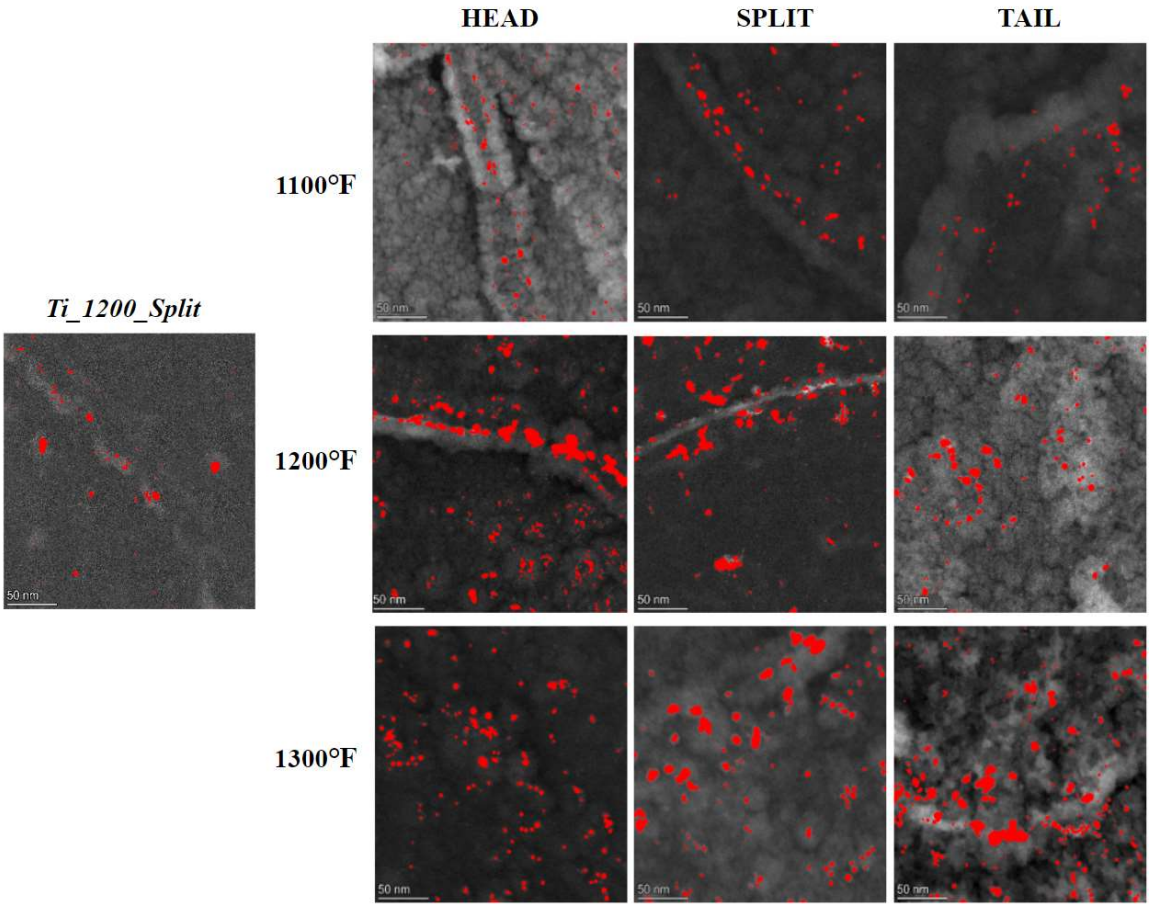

Figure 3.4.1 Representative STEM images of (Nb,Ti)C precipitates for Ti control sample and DOE samples.

Table 3.4.2 Orowan & Shear Strength Summary with 95% Propagated Error

Sample Label	Coil Temp. (°F)	Coil Location	Shear Strength (MPa)	Orowan Strength (MPa)	Total Precipitate Strength (MPa)
NbTi_1100_Head	1100	Head	84±14	125±16	150±16
NbTi_1100_Split	1100	Split	52±5	136±4	146±4
NbTi_1100_Tail	1100	Tail	49±8	131±13	140±13
NbTi_1200_Head	1200	Head	69±2	146±4	162±3
NbTi_1200_Split	1200	Split	81±4	141±5	162±4
NbTi_1200_Tail	1200	Tail	88±3	134±3	161±3
NbTi_1300_Head	1300	Head	50±4	153±6	161±6
NbTi_1300_Split	1300	Split	39±3	187±4	191±4
NbTi_1300_Tail	1300	Tail	68±6	167±4	180±4
Ti_1200_Split	1200	Split	75±5	169±6	185±6

3.5 Total Predicted Strength

The strength contribution from solid solution strengthening, Hall-Petch strengthening, dislocation strengthening, and precipitation strengthening is summed using Equation 1.2.1 and the 95% error was propagated. The base frictional lattice strength (σ_o) value of 54 MPa was used. The NbTi samples average strength is 699±9 MPa.

Table 3.5.1 Total strength summary with 95% propagated error. No error statistics for measured yield strength.

Sample Label	Solid Solution Strength (MPa)	Hall-Petch Strength (MPa)	Dislocation Strength (MPa)	Precipitate Strength (MPa)	Estimated Yield Strength (MPa)	Measured Yield Strength (MPa)
NbTi_1100_Head	45	408 ± 8	129.7 ± 0.3	150±16	705±15	658
NbTi_1100_Split	45	408 ± 5	130.3 ± 0.3	146±4	702±6	768
NbTi_1100_Tail	45	417 ± 6	127.0 ± 0.3	140±13	704±11	655
NbTi_1200_Head	46	396 ± 3	111.3 ± 0.3	162±3	693±6	709
NbTi_1200_Split	46	395 ± 5	126.5 ± 0.3	162±4	700±7	695
NbTi_1200_Tail	46	387 ± 4	110.4 ± 0.3	161±3	682±5	744
NbTi_1300_Head	47	400 ± 4	144.4 ± 0.3	161±6	717±6	661
NbTi_1300_Split	47	374 ± 5	124.6 ± 0.3	191±4	702±6	603
NbTi_1300_Tail	47	364 ± 5	122.7 ± 0.2	180±4	683±6	690
Ti_1200_Split	36	372 ± 5	98.8 ± 0.2	185±6	672±7	737

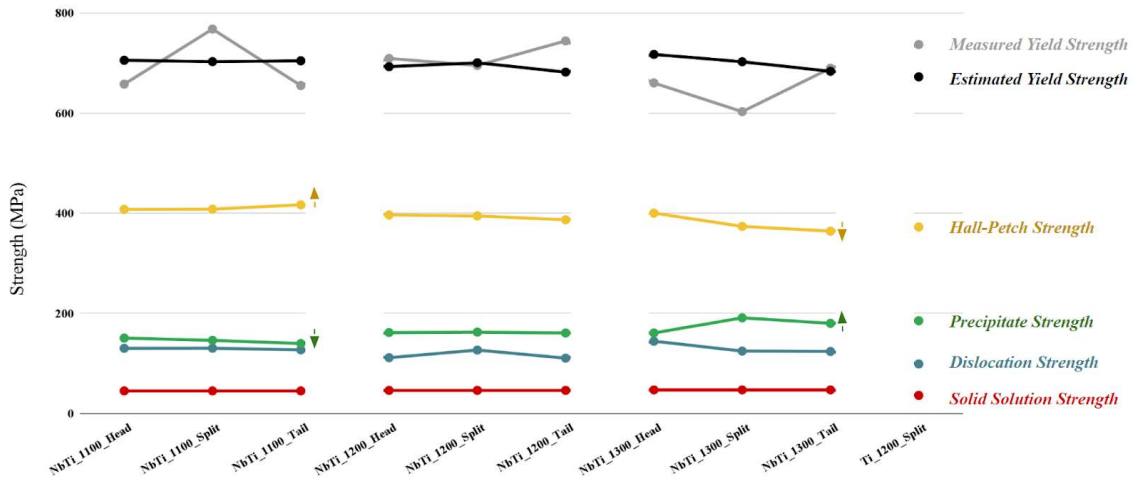

Figure 3.5.2 Line plot of average strength contribution from the four measured strengthening for each sample type. The summed strength calculated with Equation 1.2.1 is compared to the measured strength of each sample.

4 Discussion

4.1 Coil Temperature & Location Effect on Strength

4.1.1 Hall-Petch Strength

For any polycrystalline material, when there is more thermal energy available for diffusion to occur, either if that be slower cooling rates or higher hold temperatures, more grain growth via recovery or recrystallization will occur. The results of this study match this expected trend as grain size increased with increasing coil temperature and distance from the coiling mandrel (Figure 4.1.1). The coiling mandrel facilitates conductive dissipation of heat from the coil head, leading to a finer grain structure than the split and tail sections of the coil that cool by convection.

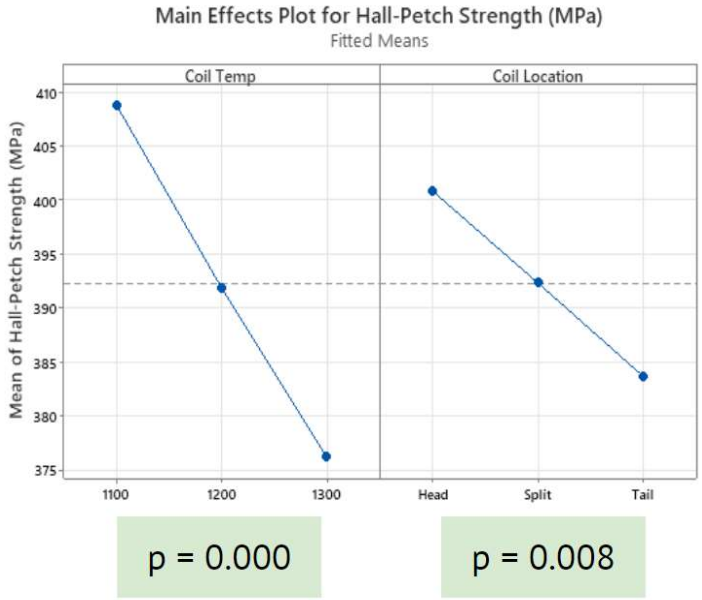

Figure 4.1.1 Main effects plots for Hall-Petch strength for DOE factors of coil temperature and coil location. Both factors had statistically significant trends with p values <0.05.

4.1.2 Dislocation Strength

Dislocation strength can be reduced as thermal energy allows for dislocations to move and recover high density dislocation regions within a grain. Therefore it is expected that dislocation strength caused by GNDs would dissipate more with increasing coiling temperature and decreased cooling rate from the coil head to tail. The expected trend for dislocation strength was observed for coil location, but not for coiling temperature (Figure 4.1.2). Dislocation strength has a significantly significant decrease (p-value=0.029) from head to tail along the length of coil.

The 1200°F DOE samples exhibited a significantly lower average strength than the 1100°F and 1300°F samples resulting in a v-shaped trend that was statistically significant (p-value=0.000). The average dislocation strength values for the 1100°F and 1300°F samples were not statistically different. There are two possible explanations to this scenario: (1) coiling process variations that the 1300°F coil experienced might have increased the retained dislocation strength in the samples or (2) coiling process variations caused the 1200°F coil to dissipate more dislocation strength and under similar conditions its dislocation strength would have also been statistically indifferent from the 1100°F and 1300°F samples. This cannot be determined without more comprehensive cooling data for the HSLA steel coils.

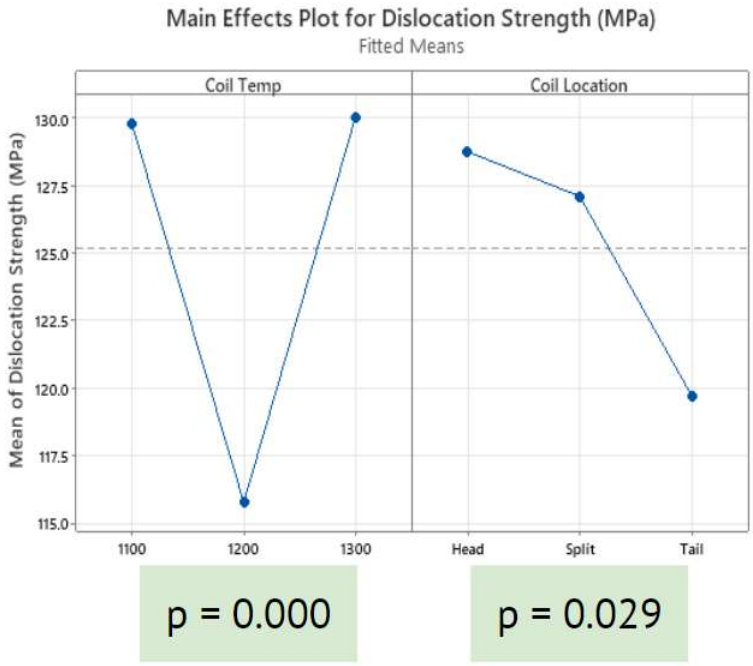

Figure 4.1.2 Main effects plots for dislocation strength for DOE factors of coil temperature and coil location. Both factors had statistically significant trends with p values <0.05.

4.1.3 Shear & Orowan Precipitate Strength

Optimizing Orowan strength is a balancing act between minimizing precipitate size to be just greater than r_{crit} and volume fraction to be maximized; for optimizing shear strength, it is desired to maximize precipitate size up to r_{crit} while maximizing volume fraction. At the appropriate temperatures for a material, these two precipitate strengthening mechanisms compliment each other by trading off strength. As coherent precipitates coarsen with higher processing temperatures past r_{crit}, they immediately start to contribute strength to Orowan strength; this helps maintain overall precipitate strength within a narrow size range within the material until incoherent precipitates grow too large to contribute strength (Figure 1.2.4).

This trade off in strength was observed in this study. Volume fraction of coherent and incoherent volume fraction of (Nb,Ti)C precipitates had a Pearson correlation value of r=-0.910 and was statistically significant with p=0.001 (Figure 4.1.3). This complemented the significant positive correlation between coil temperature and volume fraction of incoherent (Nb,Ti)C precipitates; coil temperature and coherent volume fraction had a nearly significant negative correlation. This implies that in the coiling temperature range of 1100°F to 1300°F Orowan and shear precipitate strength trade dominance to overall maintain precipitation strength in the material.

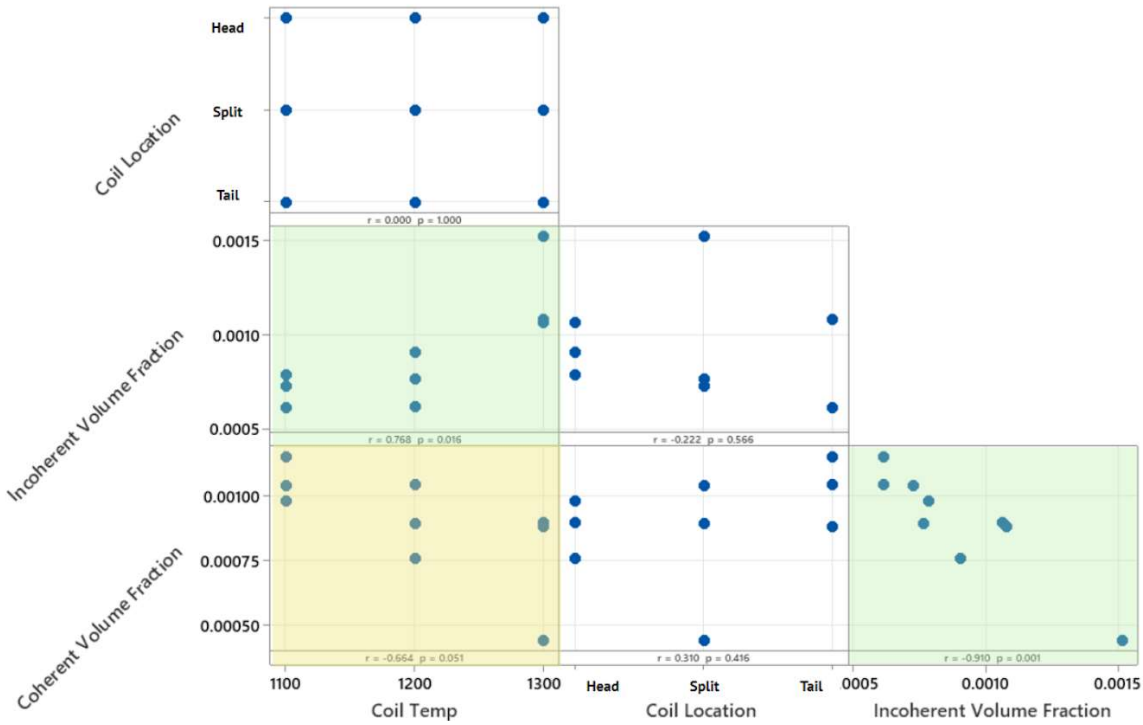

Figure 4.1.3 Correlation plot with Pearson correlation and p-value statistics for coil temperature, coil location, and volume fraction of coherent and incoherent (Nb,Ti)C precipitates. Ti_1200_Split sample was left out of this analysis. Green highlighted plots are statistically significant with p-values <0.050; the yellow highlighted plot is significant considering p-values <0.100.

There are not as conclusive trends in (Nb,Ti)C precipitate radius data for coil temperature and location (Figure 4.1.4). The only statistically significant correlation was between incoherent radius size and coil location.

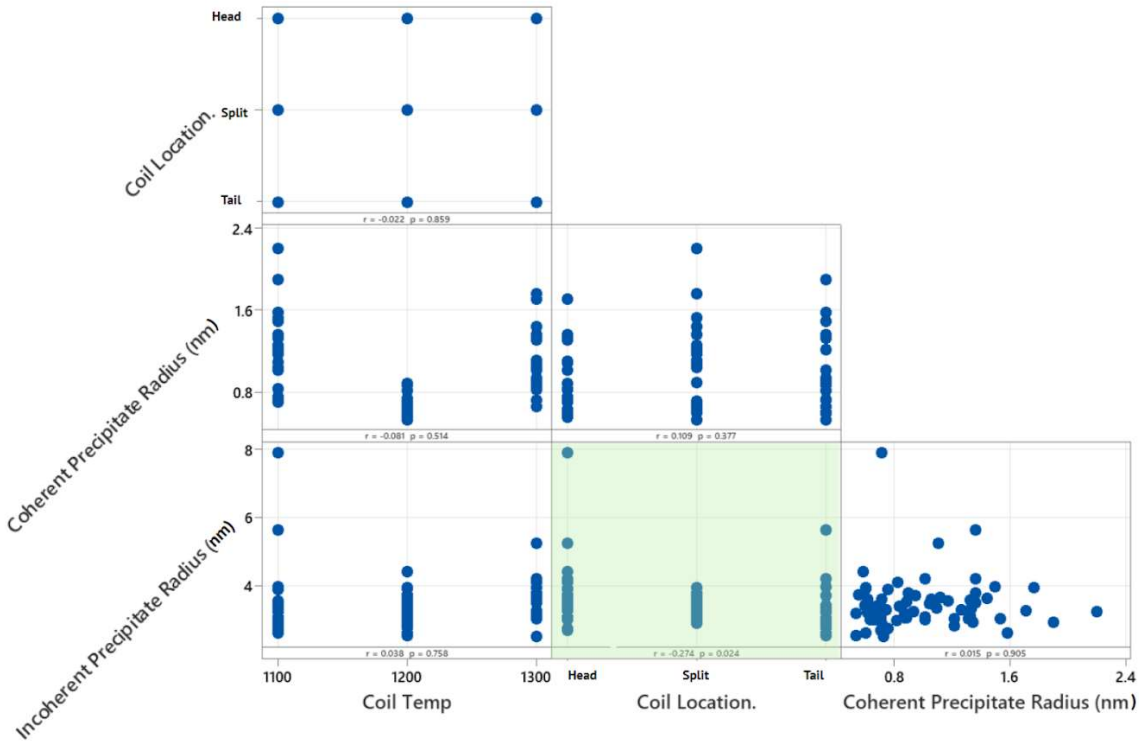

Figure 4.1.4 Correlation plot with Pearson correlation and p-value statistics for coil temperature, coil location, and precipitate radius of coherent and incoherent (Nb,Ti)C precipitates. Ti_1200_Split sample was left out of this analysis. Green highlighted plots are statistically significant with p-values <0.050.

From these correlation analyzes it can be concluded that from the data collected that the individual volume fractions of coherent and incoherent (Nb,Ti)C precipitates was more potent in determining precipitation strength contributions over precipitate radius. Orowan and shear strength contributions had a negative correlation of r=-0.296 and this trend had a p-value of 0.014 (Figure 4.1.5). Orowan strength and coil temperature had a positive correlation of r=0.634 and p=0.000.

Shear strength had an inverted "v" trend with the 1200°F having the highest shear strength; this does follow the expected trend of decrease in shear strength with increase in temperature. However, this inconsistency does mirror the one observed in 1200°F's measured dislocation strength.

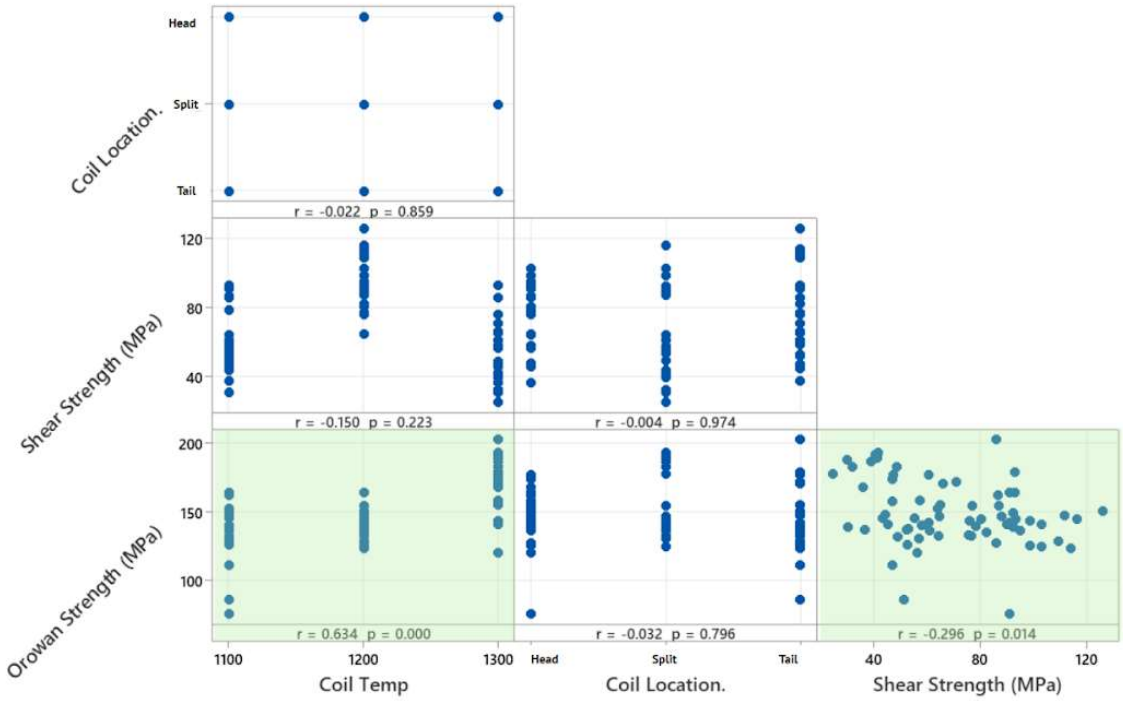

Figure 4.1.5 Correlation plot with Pearson correlation and p-value statistics for coil temperature, coil location, shear strength and Orowan strength contributed by (Nb,Ti)C precipitates. Ti_1200_Split sample was left out of this analysis. Green highlighted plots are statistically significant with p-values <0.050.

The main effects and interaction plot from the Minitab general linear model analysis of (Nb,Ti)C precipitate data shows this inverse trend clearly for the coil location (Figure 4.1.6, Figure 4.1.7). All factors and interactions were significant except for Orowan strength and coil location, although this trend is consistent with expectations. The 1200°C coil temperature is the unexpected result, and as Figure 4.1.7a shows, this coil

temperature maintains the shear strength observed at the 1100°C while all other shear strengths decrease. The peak Orowan strength at the center of the 1300°C coil makes sense, given this location on the coil could retain heat the longest while cooling.

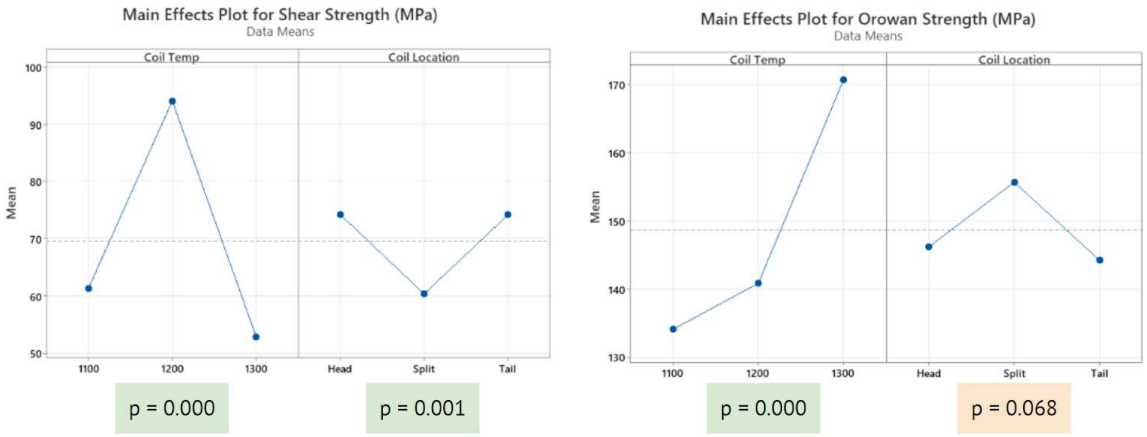

Figure 4.1.6 Main effects plots for shear and Orowan strength for DOE factors of coil temperature and coil location. Coil location did not have a statistically significant effect on Orowan strength although the observed trend agrees with expectations.

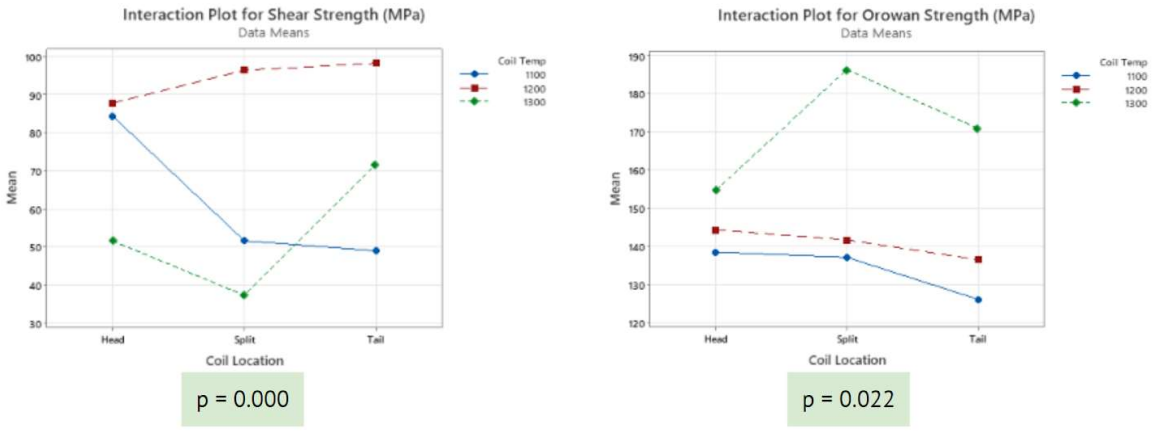

Figure 4.1.7 Interaction plots for shear and Orowan strength for DOE factors of coil temperature and coil location. Both factors had statistically significant trends with p values <0.05.

4.1.4 Summed Precipitate Strength

When assessing the pythagorean summed precipitate strength against the DOE factors, it is clear that overall precipitation strength increases with coiling temperature. Coiling location does not have a statistically significant effect on total precipitate strength. This is desired as the precipitation strength within a coil is more uniform and any variation in strength from head to tail is not from this mechanism (Figure 4.1.9).

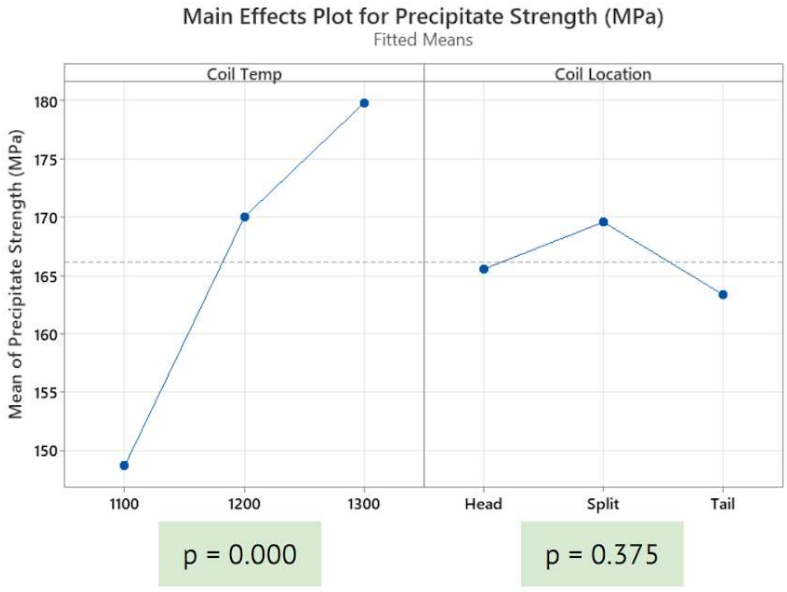

Figure 4.1.8 Main effects plots for total precipitation strength for DOE factors of coil temperature and coil location. Coil location did not have a statistically significant effect on total precipitate strength.

4.2 Hypothesis Analysis

This study hypothesized that if hot-rolled HSLA steel is micro-alloyed with niobium, then mechanical properties will be more uniform despite variations in coiling temperature because niobium will increase precipitation strengthening at higher temperatures where dislocation strength and grain size strength decrease. This theory is confirmed by a correlation analysis of the three experimentally assessed strengthening mechanisms that revealed a strong, significant, negative correlation between Hall-Petch strength and precipitation strength. No other statistically significant trends between strengthening mechanisms were found, indicating the strength trade-off between Hall-Petch and precipitation strength was the main relationship that drove uniform strength throughout the DOE conditions.

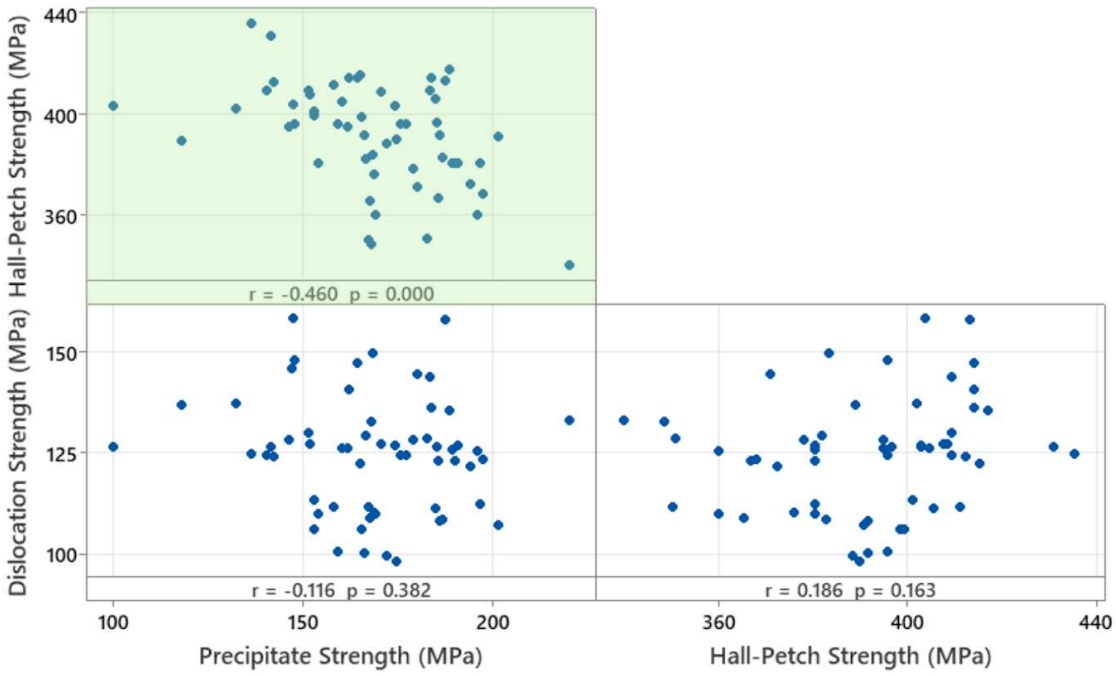

Figure 4.2.1 Correlation plot with Pearson correlation and p-value statistics for Hall-Petch, dislocation, and precipitation strength for NbTi samples. Ti_1200_Split sample was left out of this analysis. Green highlighted plots are statistically significant with p-values <0.050.

This study affirmed the hypothesis that niobium and titanium strengthen HSLA steels by increasing precipitation strength at temperatures where Hall-Petch strength decreases, and therefore provides an explanation for the small variance observed for Grade 100 NbTi HSLA steel strength distribution in Figure 1.1.5. This research can be more impactful with a secondary study that reviews titanium's effect on its own so that the reason for the large variance observed in Figure 1.1.5 for Grade 100 Ti HSLA steels can be quantified. The Ti_1200_Split sample did not provide enough insight in this study to conclude titanium's weakest strengthening mechanism contribution to hot-rolled HSLA steel.

5 Conclusions

In order for steel mini-mills and their customers to function economically and efficiently, it is crucial that produced HSLA steel bulk products meet target strength specifications. If there is a practice that minimizes strength errors stemming from mini-mill process variations, it is reasonable to conclude that the practice should be adopted to maintain proficiency.

The practice of alloying niobium in steel has been researched for decades now, and has now become a regular micro-alloying element for some HSLA steel bulk producers. This use of niobium is now justified in the quantification of microstructural trends and therefore strengthening mechanism trends occur at typical processing temperatures.

The coil temperature and coil location DOE assessed for NbTi HSLA steel samples concluded a significant, inverse trend between Hall-Petch strength and precipitation strength. Literature agrees with this observed trend as niobium has increased diffusivity in ferrite compared to other common alloying elements. Increased diffusivity allows for niobium to participate more in the nucleation and growth of (Nb,Ti)C precipitates after the austenite-to-ferrite transformation. This improves the overall strength of the material while elevated coiling temperatures cause a decrease in Hall-Petch strength by facilitating grain recovery and growth.

6 Reference List

[1] C. D. Horvath, “2 - Advanced steels for lightweight automotive structures,” in *Materials, Design and Manufacturing for Lightweight Vehicles*, P. K. Mallick, Ed., in Woodhead Publishing Series in Composites Science and Engineering. Woodhead Publishing, 2010, pp. 35–78. doi: 10.1533/9781845697822.1.35.

[2] M. Militzer, E. B. Hawbolt, and T. R. Meadowcroft, “Microstructural model for hot strip rolling of high-strength low-alloy steels,” *Metall. Mater. Trans. A*, vol. 31, no. 4, pp. 1247–1259, Apr. 2000, doi: 10.1007/s11661-000-0120-4.

[3] M. Mikolaiczik, “2021 Mustang Mach-E,” 2021. [Online]. Available: https://www.steel.org/wp-content/uploads/2021/06/GDIS-2021-_-Track-1_01_Mikolaiczik_Mustang-Mach-E-.pdf

[4] *SDI Flat Roll - Steel Making Process*, (Sep. 14, 2018). [Online Video]. Available: https://www.facebook.com/watch/?v=1709272629185043

[5] H. Yu, Q. Chen, Y. Kang, and Y. Sun, “Microstructural research on hot strips of low carbon steel produced by a compact strip production line under different thermal histories,” *Mater. Charact.*, vol. 54, no. 4, pp. 347–353, May 2005, doi: 10.1016/j.matchar.2004.12.012.

[6] K. Vanover, “Discussion with Kyle Vanover from Steel Dynamics Inc (Butler, IN) about HSLA steel grades and minimill production.,” May 30, 2023.

[7] W. D. Callister and D. G. Rethwisch, *Fundamentals of Materials Science and Engineering: An Integrated Approach, 4th Edition: An Integrated Approach*. Wiley, 2011.

[8] J. Ren and Z. Liu, “Mechanical Properties and Strength Prediction of Ti Microalloyed Low Carbon Steel with Different Ti Content,” *IOP Conf. Ser. Mater. Sci. Eng.*, vol. 611, no. 1, p. 012010, Oct. 2019, doi: 10.1088/1757-899X/611/1/012010.

[9] A. J. E. Foreman and M. J. Makin, “DISLOCATION MOVEMENT THROUGH RANDOM ARRAYS OF OBSTACLES,” *Can. J. Phys.*, vol. 45, no. 2, pp. 511–517, Feb. 1967, doi: 10.1139/p67-044.

[10] A. Sagar, “Solid Solution Strengthening | Strengthening Mechanisms | Mechanical Metallurgy,” *Learn Metallurgy*. https://learnmetallurgy.com/study/mechanical/topic/solid-solution-strengthening.php (accessed Jul. 05, 2023).

[11] “Microstructure and Mechanical Properties of HSLA-100 Steel.” Accessed: Jul. 20, 2023. [Online]. Available: https://apps.dtic.mil/sti/citations/ADA242937

[12] S. Takaki, D. Akama, N. Nakada, and T. Tsuchiyama, “Effect of Grain Boundary Segregation of Interstitial Elements on Hall–Petch Coefficient in Steels,” *Mater. Trans.*, vol. 55, no. 1, pp. 28–34, 2014, doi: 10.2320/matertrans.MA201314.

[13] W. Blum and X. H. Zeng, “A simple dislocation model of deformation resistance of ultrafine-grained materials explaining Hall–Petch strengthening and enhanced strain rate sensitivity,” *Acta Mater.*, vol. 57, no. 6, pp. 1966–1974, Apr. 2009, doi: 10.1016/j.actamat.2008.12.041.

[14] D. A. Hughes, N. Hansen, and D. J. Bammann, “Geometrically necessary boundaries, incidental dislocation boundaries and geometrically necessary dislocations,” *Scr. Mater.*, vol. 48, no. 2, pp. 147–153, Jan. 2003, doi: 10.1016/S1359-6462(02)00358-5.
[15] A. Kundu and D. P. Field, “Geometrically Necessary Dislocation Density Evolution in Interstitial Free Steel at Small Plastic Strains,” *Metall. Mater. Trans. A*, vol. 49, no. 8, pp. 3274–3282, Aug. 2018, doi: 10.1007/s11661-018-4693-1.
[16] M. Calcagnotto, D. Ponge, E. Demir, and D. Raabe, “Orientation gradients and geometrically necessary dislocations in ultrafine grained dual-phase steels studied by 2D and 3D EBSD,” *Mater. Sci. Eng. A*, vol. 527, no. 10, pp. 2738–2746, Apr. 2010, doi: 10.1016/j.msea.2010.01.004.
[17] M. Charleux, W. J. Poole, M. Militzer, and A. Deschamps, “Precipitation behavior and its effect on strengthening of an HSLA-Nb/Ti steel,” *Metall. Mater. Trans. A*, vol. 32, no. 7, pp. 1635–1647, Jul. 2001, doi: 10.1007/s11661-001-0142-6.
[18] T. Balakrishna Bhat and V. S. Arunachalam, “Strengthening mechanisms in alloys,” *Proc. Indian Acad. Sci. Sect. C Eng. Sci.*, vol. 3, no. 4, pp. 275–296, Dec. 1980, doi: 10.1007/BF02842915.
[19] M. S. Gagliano and M. E. Fine, “Precipitation kinetics of niobium carbide and copper in a low carbon, chromium-free steel,” *Calphad*, vol. 25, no. 2, pp. 207–216, Jun. 2001, doi: 10.1016/S0364-5916(01)00043-8.
[20] D. Casari, “The Grain Refinement and the Ni/V Contamination in the A356 Aluminium Casting Alloy: an Experimental Study on Impact and Tensile Properties,” 2014. doi: 10.13140/2.1.4611.0726.
[21] A. Deardo, “Niobium in modern steels,” *Int. Mater. Rev.*, vol. 48, pp. 371–402, Dec. 2003, doi: 10.1179/095066003225008833.